Title: **Mode III critical distance determination with optimized V-notched specimen under torsional fatigue and size effects on the inverse search probability distribution**

Authors: **C. Santus, F. Berto, M. Pedranz, M. Benedetti**

DOI Link: https://doi.org/10.1016/j.ijfatigue.2021.106351

Mode III critical distance determination with optimized V-notched specimen under torsional fatigue and size effects on the inverse search probability distribution

C. Santus[a,*], F. Berto[b], M. Pedranz[c], M. Benedetti[c]

[a]*Department of Civil and Industrial Engineering – DICI, University of Pisa, Italy.*
[b]*Department of Mechanical and Industrial Engineering, NTNU – Norwegian University of Science and Technology, Trondheim, Norway.*
[c]*Department of Industrial Engineering – DII, University of Trento, Italy.*

Abstract

An optimized V-notched specimen is proposed for the determination of mode III, or torsional, critical distance. Numerical procedures are provided for the inverse determination of this length, and then for a statistical analysis of the resulting skew-normal distribution, as obtained from (symmetric) normal distributions of the plain and notched specimen strengths. An experimental example is shown on steel 42CrMo4+QT, with clear evidence of a significantly larger mode III critical distance than mode I. A parametric analysis is then presented to evaluate the effects of size of the specimen on the standard deviation of the inverse search critical distance probability distribution.

Keywords: Mode III fatigue critical distance, Line Method, Point Method, Statistics, 42CrMo4+QT.

*Corresponding author: Ciro Santus
Ph. +39 (0)50 2218007
Email address: ciro.santus@ing.unipi.it (C. Santus)

Nomenclature

TCD	theory of critical distances
LM, PM	Line Method and Point Method, respectively
SED	strain energy density method
SIF	stress intensity factor
N-SIF	notch SIF
SCF	stress concentration factor
+QT	quenched and tempered (heat treatment)
CV	coefficient of variation
NCV	normalized coefficient of variation
SND	skew-normal distribution
$\bar{\alpha}$	notch opening angle
D	specimen outer diameter
R	notch radius
A	notch depth
a	dimensionless notch depth
ρ	notch radius ratio
x	V-notch bisector coordinate
ξ	dimensionless V-notch bisector coordinate
s_3	mode III power law singularity exponent
K_{N3}	N-SIF under mode III of an ideally sharp V-notched specimen
$K_{\mathrm{N3,UU}}$	N-SIF under mode III for unitary nominal stress and unitary half diameter
$\tau_{z\theta}$	shear stress induced by torsion on the V-notch bisector
$\Delta\tau_{z\theta,\mathrm{av}}$	averaged shear stress, according to the LM, full range
τ_{N}	nominal torsional stress at the V-notch section
$\Delta\tau_{\mathrm{fl}}$	plain specimen torsional fatigue limit, full range
$\Delta\tau_{\mathrm{N,fl}}$	notched specimen torsional nominal stress fatigue limit, full range
K_{fT}	fatigue stress concentration factor, under torsional loading
K_{tT}	theoretical stress concentration factor, under torsional loading
E_{K}	exponent for the K_{tT} model
$t_1, \ldots, t_4$	K_{tT} model coefficients

ΔK_{th}	mode I threshold SIF full range
$\Delta K_{\text{III,th}}$	mode III threshold SIF full range
L	LM critical distance under mode I fatigue loading
$L_{\text{T}}, L'_{\text{T}}$	critical distance under mode III, or torsional, fatigue loading, LM and PM respectively
$l_{\text{T}}, l'_{\text{T}}$	dimensionless lengths for $L_{\text{T}}, L'_{\text{T}}$, respectively
$f(l_{\text{T}}), f'(l'_{\text{T}})$	correction functions from sharp to radiused V-notched specimen, LM and PM respectively
$\gamma(l_{\text{T}}), \gamma'(l'_{\text{T}})$	inversion function, LM and PM respectively
$l_{0,\text{T}}, l'_{0,\text{T}}$	dimensionless lengths according to the singularity N-SIF term, LM and PM respectively
$l_{\text{T,min}}, l_{\text{T,int}}, l_{\text{T,max}}$	minimum, intermediate and maximum dimensionless lengths for the LM inversion
$\gamma_{\text{T,min}}, \gamma_{\text{T,int}}, \gamma_{\text{T,max}}$	LM inversion functions for $l_{\text{T,min}}, l_{\text{T,int}}, l_{\text{T,max}}$, respectively
p_{ij}	coefficients for length and LM inversion function values, $i = 1,\dots,5$ and $j = 1,\dots,4$
$l'_{\text{T,min}}, \dots, l'_{\text{T,max}}$	minimum, intermediates and maximum dimensionless lengths for the PM inversion
$\gamma'_{\text{T,min}}, \dots, \gamma'_{\text{T,max}}$	PM inversion functions for $l'_{\text{T,min}}, \dots, l'_{\text{T,max}}$, respectively
q_{ij}	coefficients for lengths and PM inversion functions, $i = 1,\dots,5$ and $j = 1,\dots,4$
$c_1, \dots, c_3$	polynomial coefficients used either for LM direct problem or inverse search
$c_1, \dots, c_5$	polynomial coefficients used either for PM direct problem or inverse search
r, r_{N}	CV of the plain and notched specimen torsional fatigue limit range, respectively
κ	r_{N} to r ratio
Σ	equivalent CV of the input data for the notch-derived critical distance estimation
$\Delta\bar{\tau}_{\text{fl}}, \Delta\bar{\tau}_{\text{N,fl}}$	mean values of the normally distributed $\Delta\tau_{\text{fl}}$ and $\Delta\tau_{\text{N,fl}}$, respectively
S, S_{N}	standard deviations of the normally distributed $\Delta\tau_{\text{fl}}$ and $\Delta\tau_{\text{N,fl}}$, respectively
$PDF(x)$	probability density function
α, β, γ	shape, location and scale parameters, respectively, of l_{T} skew-normal distribution
μ, δ, sk	mean, standard deviation and skewness parameters, respectively, of l_{T} skew-normal distribution
$\bar{l}_{\text{T}}$	critical distance obtained with mean values of plain and notched specimen torsional fatigue limits
ν	NCV of the critical distance, normalized with respect to the equivalent CV of the input data Σ
ν_0	NCV of the critical distance for an ideally sharp V-notched specimen
$l_{\text{T,lim}}$	minimum, or limit, critical distance corresponding to a given value ν of the NCV
$a_1, \dots, a_4$	coefficients of the skewness inversion function
$b_1, \dots, b_3$	coefficients of the limit critical distance model
$n_1, \dots, n_4$	coefficients of the NCV estimation model
$m_1, \dots, m_5$	coefficients of the model for the critical distance mean value over $\bar{l}_{\text{T}}$ ratio

$s_1, \ldots, s_6$	coefficients of the critical distance skewness model
$\tau_a, \tau_{N,a}$	torsional shear stress amplitudes of the plain and the notched specimens, respectively
N_f	number of cycles to failure of the plain and the notched specimen tests
k_1, k_2	Basquin's equation coefficients
d	Plain specimen diameter

1. Introduction

The fatigue verification of machine elements is crucial in engineering design. It is particularly challenging, as it has to take into account multiaxial loading conditions, stress gradients generated by geometrical discontinuities ("notches") [1, 2, 3, 4] and residual stresses produced by chemo-thermo-mechanical treatments, such as shot peening [5, 6].

A well-known approach to deal with notch stress fields is the Theory of Critical Distances (TCD) [7]. The theoretical framework of this group of notch verification methods was initially formulated for mode I type of loading only, and applied to predict both (static) brittle fracture [8, 9, 10] and fatigue failure. In the fatigue application, the critical distance was originally obtained by combining the fatigue strength of the crack, viz. the threshold stress intensity factor (SIF) range ΔK_{th}, and the plain specimen fatigue limit. On the other hand, in the brittle fracture scenario, the critical distance is usually determined by comparing the strength of two notches with different severities [10, 11, 12, 13, 14]. The TCD was recently extended to the multiaxial fatigue, by combining a multiaxial criterion, with the critical plane concept (where appropriate), and the stress averaging. The simpler Point Method is usually preferred in multiaxial fatigue, however, there are also examples with Line or Area Methods [15, 16, 17, 18, 19, 20]. A very important issue here is that the critical distance length is just considered a unique value, i.e. without distinguishing between mode I or mixed loading. Susmel and Taylor [16, 19] reported a variable critical distance as a function of the applied stress, however this variability was only intended as dependent on the (predicted) number of cycles to failure. Benedetti and Santus [21] also combined several fatigue multiaxial criteria with Point and Line Methods, and proposed different lengths, depending on the fatigue life and elastic or elastic-plastic formulation of the multiaxial criterion. Importantly, after fixing criterion and fatigue life, a unique material critical distance was assumed regardless of the degree of stress multiaxiality. An interesting application with multiaxial variable stresses is the fretting fatigue. In several examples in the literature [22, 23, 24, 25], the TCD was used to consider high gradient stresses, in combination with different criteria, mainly the Modified WÃűhler Curve Method (MWCM), the Fatemi-Socie (FS) and the Smith-Watson-Topper (SWT) criteria. Even in the fretting application, just a unique TCD length was assumed, which is obviously the

length obtained from mode I type of loading, despite the high level of shear stresses induced by the local friction. As already mentioned, to estimate the critical distance under fatigue loading, the (mode I) threshold and the plain specimen fatigue limit are required. However, the determination of ΔK_{th} requires specific equipment and expertise. For this reason, the fatigue critical distance length is more easily determined by imposing a TCD condition and combining the plain specimen fatigue limit and the strength of a sharply notched specimen. The authors [26, 27, 28] recently proposed and validated the use of a dedicated V-notched round specimen, with optimized notch depth, and a radius as small as possible, still maintaining the manufacturing accuracy. In combination with this dedicated specimen, an analytical procedure for the fatigue critical distance determination was also provided. A numerical procedure was again proposed by the authors [29] for the statistical distribution of the critical distance obtained with this method, by assuming both the plain and the V-notched specimen fatigue strengths as normal (or Gaussian) distributions.

A similar approach for predicting both fatigue and fracture, also under mixed mode loading conditions, is the strain energy density (SED), which is averaged over a structural volume whose characterized size is a material-dependent parameter, usually referred to as the control radius [30, 31, 32]. A similar procedure used to determine the fatigue SED control radius by the authors [33] for mode I. To extend SED to multiaxial fatigue scenarios, two different control radii were postulated and found for in-plane and out-of-plane loadings [34, 35, 36, 37, 38, 39]. A larger mode III radius than mode I was experimentally observed, which could be attributed to the possibly higher threshold SIF range under out-of-plane loading. This in turn can be explained as the synergistic effect of an intrinsic material strength and an extrinsic crack shielding mechanism, which is induced by typical factory-roof crack surfaces [31]. The extrinsic component is not exclusive to mode III loading. In fact, it is well-known that the plasticity induced crack closure mechanism introduces another extrinsic component under mode I loading [40, 41, 42], and the crack surface roughness-induced closure is typical of mode II [40]. However under mode III, this contact shielding is dominant, as pointed out by Yu et al. [43]. After accepting that values of the mode I and mode III critical radii are quite different, the SED can be applied just by summing the two contributions in terms of energy, averaged over two domains with different radii [34, 44, 45].

Similarly to the SED method, two different TCD lengths can in principle be defined, namely the mode I and mode III critical distances. Susmel and Taylor [46] postulated a mode III critical distance L_T, obtained from torsional mechanical tests. From the literature data, they found that L_T is usually larger than L which is the (classical) mode I length, and their ratio is approximately in the range $L/L_T = 0.3 - 0.6$. Susmel and Taylor [11] also found a similar ratio L/L_T for PMMA (polymethyl methacrylate) under brittle fracture, by combining two different notches, as previously discussed, also for torsional loading. In terms of SED, Berto et al. [31] found for 39NiCrMo3 steel, 0.327 mm and 1.426 mm for mode I and mode III control radii, respectively. Berto et al.

[34] reported 0.051 mm and 0.837 mm for Ti-6Al-4V alloy. Thus, similarly to L_T, the mode III control radius resulted much larger than its mode I counterpart.

In agreement with the L definition, as discussed by Susmel and Taylor [47], L_T should in principle be derived from the SIF threshold range:

$$L_T = \frac{1}{\pi}\left(\frac{\Delta K_{III,th}}{\Delta \tau_{fl}}\right)^2, \quad \Delta K_{III,th} = ? \tag{1}$$

However, $\Delta K_{III,th}$ is not accessible from an experimental point of view, mainly because of the instability initial propagation of the crack [48, 49]. There is in fact no standardized procedure, such as the well-known ASTM E647 for mode I fatigue crack growth tests, to determine $\Delta K_{III,th}$. For this reason, as suggested in Ref. [47], the same mode III and mode I lengths can be considered. This simple assumption is conservative because, as mentioned before, the mode I critical distance is smaller than L_T, thus higher averaged mode III stresses are expected. For a more accurate mode III fatigue calculation, in this work we propose the extension of the inverse search procedure of L_T, based on a dedicated notched specimen geometry, as in our past article [26]. The value of L_T can thus be used for the back-calculation of the mode III threshold $\Delta K_{III,th}$ after inverting Eq. 1. A round notched specimen is recommended here, since for other geometries edge effects arise at the notch boundaries [50, 51, 52] which are inappropriate for this inverse search target. In addition, a further procedure determines the statistical distribution of the length L_T itself, after assuming Gaussian (or normal) distributions for the fatigue limits of the two plain and notched specimens involved.

In the final part of this work, the effects of the size of the specimen on the mode III critical distance determination are investigated and compared to mode I. A recent approach to the size effect considers the critical distance dependent not only on the material, but also on the notch size [53, 54]. On the other hand, a different probabilistic perspective only considers the fatigue limit as dependent on the size [55, 56, 57]. In agreement with this latter assumption, the critical distance is not assumed here as being dependent on the dimensions of the specimens. However, the size effect is investigated in terms of the inverse search reliability, in particular regarding the mode III length. The ratio between the standard deviation over mean value, of the predicted critical distance, and that of the (combined) input fatigue properties, is assumed as an assessment index for the inversion search accuracy. This parameter is more precisely defined below as the normalized coefficient of variation (NCV), and its dependences on the critical distance size, the notch radius, and the specimen outer diameter, are investigated and discussed.

2. Optimal specimen definition

The most effective shape to determine the mode III critical distance is a round specimen loaded under torsion and with a sharp axisymmetric V-notch. Plate or disc shapes, under anti-plane loading, are not recommended because a nonuniform distribution and high gradient of K_{III} is obtained at the edges, as investigated by Pook, Campagnolo and Berto [51, 52]. An alternative notch shape, such as a U-notch, is also ineffective in this context, as a very small notch radius cannot be manufactured, at least not with conventional machining.

The definition of the specimen dimensions along with the shear stress component, induced by the torsion, are reported in Fig. 1. In this work the whole notch opening angle is referred to as $\bar{\alpha}$. The outer diameter of the specimen is D, the notch radius is R, and the notch depth is A. The parameters of the specimen can be put in dimensionless form for a more efficient evaluation of the geometry dependences:

$$\begin{aligned} a &= A/(D/2) \\ \rho &= R/A \end{aligned} \tag{2}$$

The shear stress along a radius at the bisection plane of the specimen is $\tau_{z\theta}$, and as this radius is on two planes of load antisymmetry, this stress component is the only active. And this is similar to the mode I loading for which σ_y is the dominant stress. The nominal shear stress follows the well-known triangular distribution, which undergoes a stress concentration at the notch root. The stress is singular here if a local zero radius is assumed, at least according to the linear elastic material behaviour, while the torsional stress concentration factor (SCF) K_{tT} can be introduced for the radiused notch.

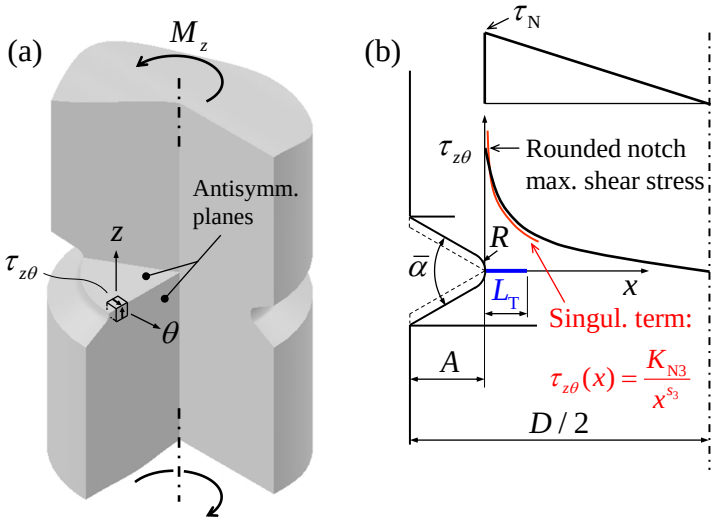

Figure 1: (a) Shear stress along the radial direction, induced by torsion. (b) Specimen dimensions, scheme with exaggerated notch radius and length L_T.

2.1. Singularity exponent

A complete formulation of different types of V-notches in round specimens under torsion can be found in Zappalorto et al. [58]. By assuming a zero radius, the shear stress (mode III) singularity power law exponent s_3, is usually expressed as the complementary to the main eigenvalue root of the singular problem λ_3, and can be easily solved for any notch open angle $\bar{\alpha}$:

$$s_3 = 1 - \lambda_3 = \frac{1 - \bar{\alpha}/\pi}{2 - \bar{\alpha}/\pi} \tag{3}$$

and in the following formulations the exponent s_3 is only used instead of λ_3.

The simple Eq. 3 is mapped in Fig. 2. When the opening angle is zero, the crack solution is attained, thus $s_3 = 0.5$, which is the classical crack singularity. However, as opposed to the mode I singularity exponent, s_3 decays relatively fast, thus leading to weak singularities for quite large angles.

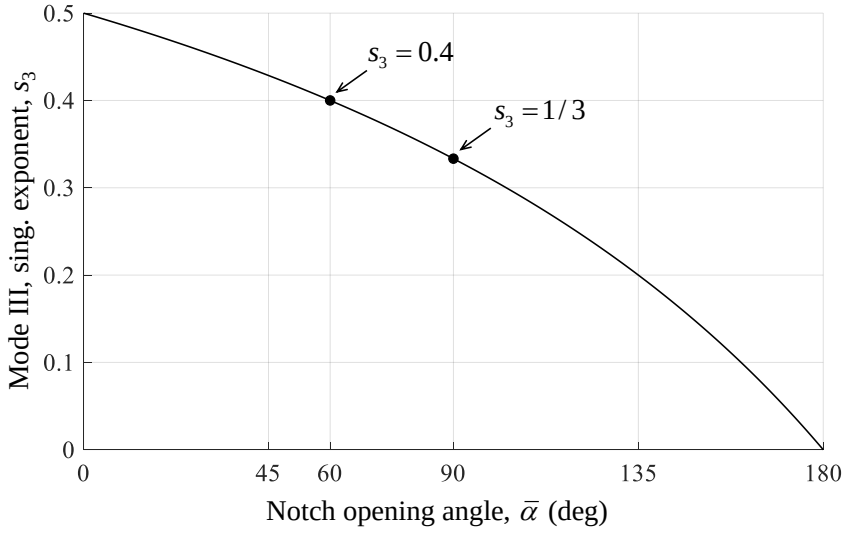

Figure 2: Mode III singularity exponent s_3 as a function of the notch opening angle $\bar{\alpha}$.

Similarly to Santus et al. [26], after having the singularity exponent available, the shear stress singular term can be easily formulated as:

$$\tau_{z\theta}(\xi) = \tau_{\mathrm{N}} \frac{K_{\mathrm{N3,UU}}}{\xi^{s_3}} \tag{4}$$

where the dimensionless coordinate $\xi = x/(D/2)$ is introduced. The Notch-SIF (N-SIF) $K_{\mathrm{N3,UU}}$ refers to mode III, and can be defined as K_{N3}, shown in Fig. 1, for a unitary radius specimen ($D/2 = 1$) and also unitary nominal stress τ_{N}.

Two notch angles $\bar{\alpha} = 60^\circ$ and $\bar{\alpha} = 90^\circ$ were investigated, which are the most common V-notch angles. The $K_{\mathrm{N3,UU}}$ was found by fitting FE simulations for different values of notch depths a. Two different maxima, though quite close, were found at the two values $a = 0.25$ and $a = 0.2$, for $\bar{\alpha} = 60^\circ$ and $\bar{\alpha} = 90^\circ$, respectively, see Fig.

Table 1: Singular term optimum notch depths, exponents and dimensionless N-SIFs.

Notch angle $\bar{\alpha}$	Optimal notch depth a	Singularity exponent s_3	Dimensionless N-SIF $K_{\mathrm{N3,UU}}$
60°	0.25	0.4	0.31861
90°	0.2	0.33333	0.40804

3.

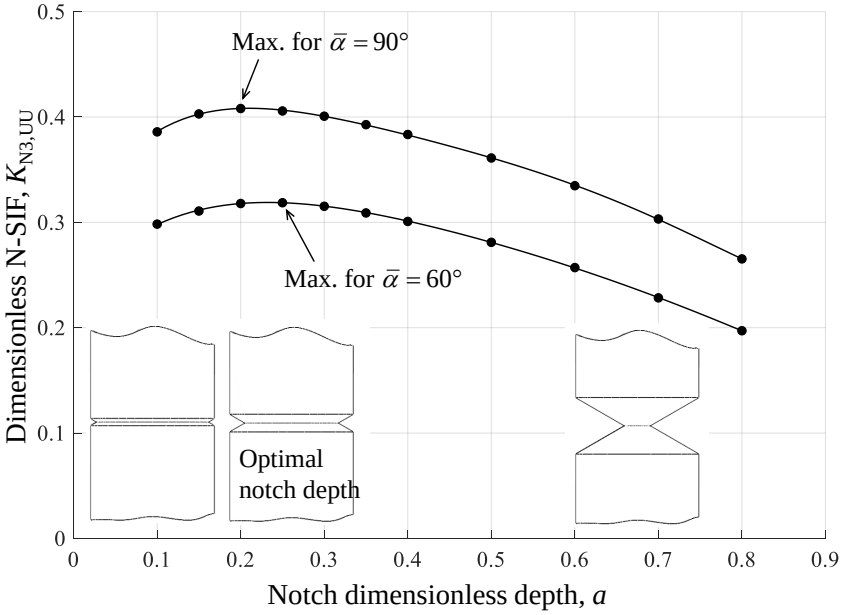

Figure 3: Optimization of the notch depth, different maxima for the two notch angles considered.

The element type used in the FE model was Plane183 in the Ansys software library. Despite this element type being bidimensional, the rotation degree of freedom along the axisymmetric direction (global Y) was activated, thus enabling the torsional loading to be modelled. A very refined mesh was applied to these simulations, being the numerical basis for the entire procedure, similarly to the accurate FE model introduced and described by the authors in Ref. [26].

3. Calculation procedure for the critical distance

A vanishingly small radius at the notch root is not possible, from the manufacturing point of view, in fact the turning tool nose determines the minimum radius that can be obtained. The assumption that this radius is at least one order of magnitude smaller that the critical distance to be determined, is not well supported by the evidence. The radius parameter was thus introduced, and its effect analysed. Using another dedicated set of accurate FE analyses, after imposing the optimal notch depths previously found for each angle, the torsional shear stress distributions were obtained, and the modelling reported below was based on this set of simulations. The ρ values investigated were: $0.01, 0.02, 0.05, 0.1, 0.2, 0.5, 1.0$ including any realistic notch radius ratio.

Table 2: Coefficients to determine the torsional SCF K_{tT}.

$\bar{\alpha}$	t_1	t_2	t_3	t_4
60°	0.019956	0.10339	-0.21129	0.13357
90°	0.013415	0.064888	-0.22451	0.15526

3.1. Radiused specimen stress concentration factor

The maximum shear stress at the notch root was easily converted into the torsional SCF, here referred to as K_{tT}. This SCF depends on the notch radius ratio ρ, which is the only remaining variable. An efficient fit form was found with a polynomial on logarithm coordinates. Eq. 5, and the t_i coefficients are listed in Table 2.

$$\begin{aligned} E_{\mathrm{K}} &= t_1(\bar{\alpha})\,(\log_{10}\rho)^3 + t_2(\bar{\alpha})\,(\log_{10}\rho)^2 + t_3(\bar{\alpha})\,\log_{10}\rho + t_4(\bar{\alpha}) \\ K_{\mathrm{tT}} &= 10^{E_{\mathrm{K}}} \end{aligned} \tag{5}$$

This K_{tT} obviously represents a maximum value for the (mode III) fatigue SCF: K_{fT}, thus corresponding to a vanishingly small critical distance.

3.2. Line Method inverse search

By following the same steps proposed by us in Ref. Santus et al. [26], the dimensionless critical distances can be defined as: $l_{\mathrm{T}} = L_{\mathrm{T}}/(D/2)$ and $l'_{\mathrm{T}} = L'_{\mathrm{T}}/(D/2)$ for the Line and Point Methods, respectively. According to the stress distribution of Eq. 4, it is possible to evaluate the dimensionless lengths based on the singularity assumption, initially proposed here for the LM:

$$\Delta\tau_{z\theta,\mathrm{av}} = \frac{1}{2\,l_{\mathrm{T}}}\int_0^{2\,l_{\mathrm{T}}} \Delta\tau_{z\theta}(\xi)\mathrm{d}\xi = \Delta\tau_{\mathrm{N}}\frac{1}{1-s_3}\frac{K_{\mathrm{N3,UU}}}{(2\,l_{0,\mathrm{T}})^{s_3}} \tag{6}$$

This average stress is then imposed that is equal to the plain specimen fatigue limit: $\Delta\tau_{z\theta,\mathrm{av}} = \Delta\tau_{\mathrm{fl}}$. Hence:

$$K_{\mathrm{fT}} = \frac{\Delta\tau_{\mathrm{fl}}}{\Delta\tau_{\mathrm{N,fl}}} = \frac{1}{1-s_3}\frac{K_{\mathrm{N3,UU}}}{(2\,l_{0,\mathrm{T}})^{s_3}} \tag{7}$$

where $\Delta\tau_{\mathrm{fl}}$ and $\Delta\tau_{\mathrm{N,fl}}$ are the plain specimen and the notched specimen fatigue limits, referring to the nominal stress. In this section, these fatigue properties are simplistically considered as deterministic variables, while they are assumed as random variables below.

The inversion of Eq. 7 can be easily solved in order to have $l_{0,\mathrm{T}}$ as output:

$$l_{0,\mathrm{T}} = \frac{1}{2}\left(\frac{K_{\mathrm{N3,UU}}}{(1-s_3)K_{\mathrm{fT}}}\right)^{1/s_3} \tag{8}$$

In principle, this length could be considered as an approximate evaluation of the torsional critical distance. However, as shown below, when the actual critical distance is quite small, the relative size of the notch radius limits the stress gradient, and consequently the preliminary length $l_{0,\mathrm{T}}$ may be not sufficiently accurate.

After introducing the radius, the local stress distribution and the LM average can be reformulated, as the result according to the singularity solution times a correction function $f(l_{\mathrm{T}})$:

$$\Delta\tau_{z\theta,\mathrm{av}} = \frac{1}{2l_{\mathrm{T}}}\int_0^{2l_{\mathrm{T}}} \Delta\tau_{z\theta}(\xi)\mathrm{d}\xi = \Delta\tau_{\mathrm{N}}\frac{f(l_{\mathrm{T}})}{1-s_3}\frac{K_{\mathrm{N3,UU}}}{(2l_{\mathrm{T}})^{s_3}} \tag{9}$$

The K_{fT} can be again introduced:

$$K_{\mathrm{fT}} = \frac{f(l_{\mathrm{T}})}{1-s_3}\frac{K_{\mathrm{N3,UU}}}{(2l_{\mathrm{T}})^{s_3}} \tag{10}$$

and after the definition of an inversion function $\gamma(l_{\mathrm{T}})$:

$$\gamma(l_{\mathrm{T}}) = \frac{l_{\mathrm{T}}}{f(l_{\mathrm{T}})^{1/s_3}} \tag{11}$$

Equation 10 can be reduced to the relationship below which is then solved in l_{T}, and this represents the inverse search problem:

$$\gamma(l_{\mathrm{T}}) = l_{0,\mathrm{T}} \tag{12}$$

In order to have a reliable modelling of this inversion function $\gamma(l_{\mathrm{T}})$, the inverse search was limited to a range $l_{\mathrm{T,min}} - l_{\mathrm{T,max}}$, and this range was then verified as including all the realistic geometry conditions. As shown in Fig. 4, the singular term LM averaging stress was assumed as a reference.

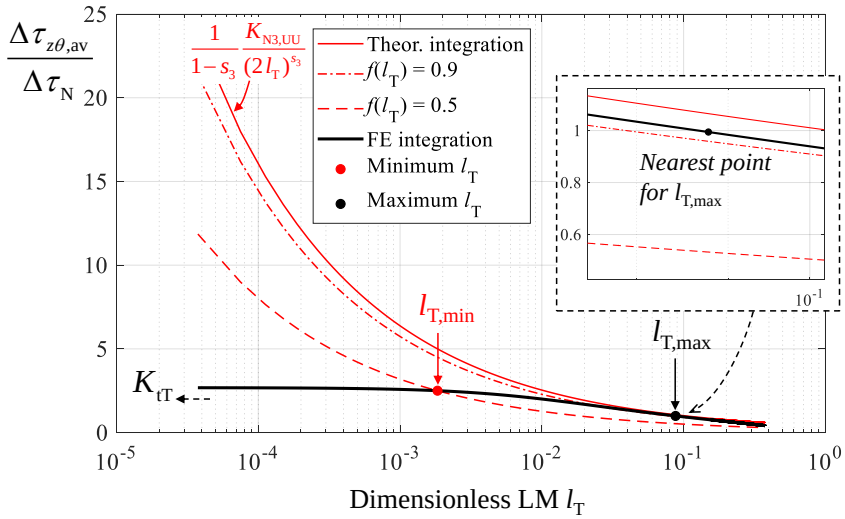

Figure 4: Maximum and minimum lengths for l_{T}, example for $\bar{\alpha} = 60°$ and $\rho = 0.1$.

The singular term stress averaging, reduced by a correction function imposed at $f(l_{\mathrm{T}}) = 0.5$, was compared with the FE result for unitary nominal stress. The minimum length $l_{\mathrm{T,min}}$ was thus defined and found. The averaged stress for any smaller l_{T}, obviously tends to the finite SCF while the singular term increases indefinitely. On the other hand, for large l_{T}, the singular and FE averaged stresses tend to be similar, meaning that the stress gradient

Table 3: Coefficients p_{ij} for the determination of the LM inversion search lengths.

p_{ij} for $\bar{\alpha} = 60°$				
	$j=1$	$j=2$	$j=3$	$j=4$
$i=1$	6.8902E−03	−1.6930E−02	1.9492E−02	3.5833E−05
$i=2$	−4.9067E−02	−2.8340E−02	2.4022E−01	2.3624E−01
$i=3$	3.9260E−02	−9.6279E−02	1.1055E−01	1.5262E−04
$i=4$	−1.3355E−02	−3.3115E−02	1.6007E−01	3.5766E−01
$i=5$	−4.2072E−02	−6.2649E−02	3.0248E−01	2.9823E−01
p_{ij} for $\bar{\alpha} = 90°$				
	$j=1$	$j=2$	$j=3$	$j=4$
$i=1$	1.6541E−03	−4.9747E−03	8.7262E−03	−5.5895E−06
$i=2$	−1.3928E−02	−4.0247E−02	1.9014E−01	3.9144E−01
$i=3$	1.2120E−02	−3.7784E−02	6.8822E−02	1.5337E−05
$i=4$	−3.4668E−03	−4.8702E−02	1.5578E−01	5.3637E−01
$i=5$	−8.6222E−03	−1.0305E−01	3.0090E−01	5.1670E−01

in that region is going down. The $l_{\mathrm{T,max}}$ was assumed at the critical distance value where the gap between these two functions is minimum. The FE averaged stress never exceeded the singular stress average, being however very close at $l_{\mathrm{T,max}}$. However, for mode I, there is always a length where the FE averaged stress is equal to the singular stress, because the stress away from the notch region tends to a uniform distribution.

The determination of $l_{\mathrm{T,min}}$ and $l_{\mathrm{T,max}}$ was repeated for all the investigated ρ and for both notch angles. The inversion functions γ_{min} and γ_{max} for each of these $l_{\mathrm{T,min}}$ and $l_{\mathrm{T,max}}$, were evaluated on the basis of the FE results. An intermediate length: $l_{\mathrm{T,int}} = (l_{\mathrm{T,min}} + l_{\mathrm{T,max}})/2$ was also evaluated for a more effective inverse model, and the corresponding γ_{int} was also found for the length $l_{\mathrm{T,int}}$. The γ values obtained were then fitted with respect to the notch radius ratio ρ variable. The proposed fit models, which were found to provide a satisfying accuracy, are reported in Eqs. 13 and 14, and the calibrated p_{ij} coefficients are listed in Table 3.

$$\begin{aligned} l_{\mathrm{T,min}} &= p_{11}(\bar{\alpha})\,\rho^3 + p_{12}(\bar{\alpha})\,\rho^2 + p_{13}(\bar{\alpha})\,\rho + p_{14}(\bar{\alpha}) \\ l_{\mathrm{T,max}} &= p_{21}(\bar{\alpha}) + p_{22}(\bar{\alpha})\,\rho + p_{23}(\bar{\alpha})\,\rho^{p_{24}(\bar{\alpha})} \\ l_{\mathrm{T,int}} &= (l_{\mathrm{T,max}} + l_{\mathrm{T,min}})/2 \end{aligned} \tag{13}$$

$$\begin{aligned} \gamma_{\mathrm{min}} &= p_{31}(\bar{\alpha})\,\rho^3 + p_{32}(\bar{\alpha})\,\rho^2 + p_{33}(\bar{\alpha})\,\rho + p_{34}(\bar{\alpha}) \\ \gamma_{\mathrm{int}} &= p_{41}(\bar{\alpha}) + p_{42}(\bar{\alpha})\,\rho + p_{43}(\bar{\alpha})\,\rho^{p_{44}(\bar{\alpha})} \\ \gamma_{\mathrm{max}} &= p_{51}(\bar{\alpha}) + p_{52}(\bar{\alpha})\,\rho + p_{53}(\bar{\alpha})\,\rho^{p_{54}(\bar{\alpha})} \end{aligned} \tag{14}$$

As mentioned above, Eq. 12 can be actually considered the *inversion* search problem, meaning that l_{T} is the unknown, and $l_{0,\mathrm{T}}$ is the input, after having elaborated K_{fT} with Eq. 8. This approach is the ultimate target of this procedure, when the experimental test results are available and l_{T} is required. However, $l_{\mathrm{T}} - \gamma$ mapping can also be used when l_{T} is known, in which case $l_{0,\mathrm{T}}$ is found and finally K_{fT} obtained with Eq. 7. This situation is

referred to here as the *direct* problem.

The effectiveness of different types of modelling was tested on the FE data, and it was found that the direct problem can be solved by interpolating the three points with a parabola:

$$l_{0,\mathrm{T}} = c_1 + c_2\, l_{\mathrm{T}} + c_3\, l_{\mathrm{T}}^2 \tag{15}$$

while for the inverse search problem, a polynomial with a non-integer value (equal to 1.5), for the highest exponent, was found to be more effective:

$$l_{\mathrm{T}} = c_1 + c_2\, l_{0,\mathrm{T}} + c_3\, l_{0,\mathrm{T}}^{1.5} \tag{16}$$

In Eqs. 15 and 16, the coefficients c_1, c_2, c_3 are obviously not the same, however, the same symbols are used for convenience. These coefficients, either for the direct problem or the inverse search, can be found by imposing the model on the available couples $l_{0,\mathrm{T}} - l_{\mathrm{T}}$, which can be quickly obtained by inverting a Vandermonde matrix even with non-integer exponents. The Vandermonde matrices for the direct problem and the inverse search are reported in Eqs. 17 and 18, respectively:

$$\begin{pmatrix} c_1 \\ c_2 \\ c_3 \end{pmatrix} = \begin{pmatrix} 1 & l_{\mathrm{T,min}} & l_{\mathrm{T,min}}^2 \\ 1 & l_{\mathrm{T,int}} & l_{\mathrm{T,int}}^2 \\ 1 & l_{\mathrm{T,max}} & l_{\mathrm{T,max}}^2 \end{pmatrix}^{-1} \begin{pmatrix} \gamma_{\mathrm{min}} \\ \gamma_{\mathrm{int}} \\ \gamma_{\mathrm{max}} \end{pmatrix} \tag{17}$$

$$\begin{pmatrix} c_1 \\ c_2 \\ c_3 \end{pmatrix} = \begin{pmatrix} 1 & \gamma_{\mathrm{min}} & \gamma_{\mathrm{min}}^{1.5} \\ 1 & \gamma_{\mathrm{int}} & \gamma_{\mathrm{int}}^{1.5} \\ 1 & \gamma_{\mathrm{max}} & \gamma_{\mathrm{max}}^{1.5} \end{pmatrix}^{-1} \begin{pmatrix} l_{\mathrm{T,min}} \\ l_{\mathrm{T,int}} \\ l_{\mathrm{T,max}} \end{pmatrix} \tag{18}$$

The coefficients obtained c_1, c_2, c_3 depend only on the notch angle $\bar{\alpha}$ and the radius ratio ρ, thus they are uniquely defined by the specimen shape, regardless of the size D. A very accurate modelling with the proposed polynomials is evident in Fig. 5, where the trends obtained are directly compared to the FE results for a certain radius ratio ρ and angle $\bar{\alpha}$, and similar results are obtained for all the other geometries.

3.3. Point Method inverse search

A similar formulation is possible for the Point Method. By implementing the PM condition, the initial length based on the singular term $l'_{0,\mathrm{T}}$ can be related to the K_{fT}:

$$l'_{0,\mathrm{T}} = 2\left(\frac{K_{\mathrm{N3,UU}}}{K_{\mathrm{fT}}}\right)^{1/s_3} \tag{19}$$

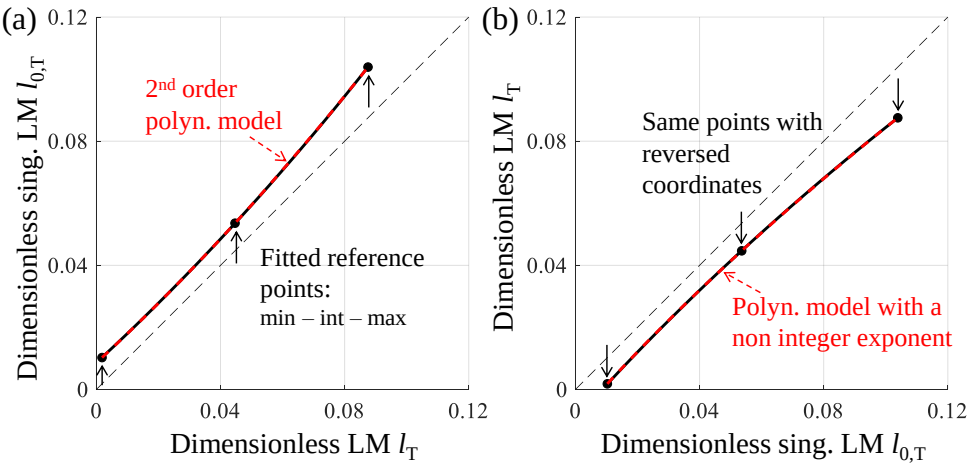

Figure 5: Line Method (a) direct problem and (b) inverse search for $\rho = 0.1$ and $\bar{\alpha} = 60°$.

On the basis of the FE stress distribution, the PM dimensionless critical distance l'_T can be put into relationship to K_{fT}, using another correction function $f'(l'_T)$, and then the two lengths $l'_{0,T} - l'_T$ can be related:

$$K_{fT} = f'(l'_T)\frac{K_{N3,UU}}{(l'_T/2)^{s_3}} = \frac{K_{N3,UU}}{(l'_{0,T}/2)^{s_3}} \tag{20}$$

After the definition of an analogous inversion function, $\gamma'(l'_T)$:

$$\gamma'(l'_T) = \frac{l'_T}{f'(l'_T)^{1/s_3}} \tag{21}$$

the inverse search can be again formulated, exactly in the same form of the LM:

$$\gamma'(l'_T) = l'_{0,T} \tag{22}$$

Due to the higher variation of this latter inversion function, another two intermediate lengths were required, as reported in Eq. 23, while the maximum and minimum lengths were assumed to be the same as those of the LM:

$$\begin{aligned} l'_{T,min} &= l_{T,min} \\ l'_{T,max} &= l_{T,max} \\ l'_{T,int} &= l_{T,int} \\ l'_{T,1} &= (l'_{T,int} + l'_{T,min})/2 \\ l'_{T,3} &= (l'_{T,max} + l'_{T,int})/2 \end{aligned} \tag{23}$$

Table 4: Coefficients q_{ij} for the determination of the PM inversion search lengths.

q_{ij} for $\bar{\alpha} = 60°$				
	$j=1$	$j=2$	$j=3$	$j=4$
$i=1$	3.8218E−02	−9.5322E−02	1.1342E−01	1.3923E−04
$i=2$	1.5707E−03	−4.1250E−02	1.1133E−01	6.2170E−01
$i=3$	−1.0494E−02	−5.5582E−03	1.0516E−01	3.0922E−01
$i=4$	−5.7542E−02	−5.1620E−03	1.7165E−01	1.6582E−01
$i=5$	−1.6157E−01	−1.2746E−02	3.0575E−01	1.0109E−01
q_{ij} for $\bar{\alpha} = 90°$				
	$j=1$	$j=2$	$j=3$	$j=4$
$i=1$	1.2941E−02	−4.1026E−02	7.6834E−02	2.0556E−05
$i=2$	5.9994E−04	−4.1773E−02	1.0597E−01	7.1174E−01
$i=3$	−3.4284E−03	−1.1135E−02	9.8204E−02	4.6516E−01
$i=4$	−1.0763E−02	−1.6730E−02	1.3296E−01	3.8161E−01
$i=5$	−1.8165E−02	−3.1322E−02	1.7997E−01	3.5741E−01

The values for the PM inversion function, corresponding to the five lengths $l'_{\mathrm{T,min}}, \ldots, l'_{\mathrm{T,min}}$, were fitted and made available with the models of Eq. 24, and the coefficients q_{ij} are reported in Table 4

$$\begin{aligned}
\gamma'_{\min} &= q_{11}(\bar{\alpha})\rho^3 + q_{12}(\bar{\alpha})\rho^2 + q_{13}(\bar{\alpha})\rho + q_{14}(\bar{\alpha}) \\
\gamma'_{1} &= q_{21}(\bar{\alpha}) + q_{22}(\bar{\alpha})\rho + q_{23}(\bar{\alpha})\rho^{q_{24}(\bar{\alpha})} \\
\gamma'_{\mathrm{int}} &= q_{31}(\bar{\alpha}) + q_{32}(\bar{\alpha})\rho + q_{33}(\bar{\alpha})\rho^{q_{34}(\bar{\alpha})} \\
\gamma'_{3} &= q_{41}(\bar{\alpha}) + q_{42}(\bar{\alpha})\rho + q_{43}(\bar{\alpha})\rho^{q_{44}(\bar{\alpha})} \\
\gamma'_{\max} &= q_{51}(\bar{\alpha}) + q_{52}(\bar{\alpha})\rho + q_{53}(\bar{\alpha})\rho^{q_{54}(\bar{\alpha})}
\end{aligned} \tag{24}$$

The direct problem can be implemented by interpolating the five points with a 4^{th} degree polynomial:

$$l'_{0,\mathrm{T}} = c_1 + c_2 l'_{\mathrm{T}} + c_3 l'^2_{\mathrm{T}} + c_4 l'^3_{\mathrm{T}} + c_5 l'^4_{\mathrm{T}} \tag{25}$$

while for the inverse problem, the use of non-integer exponents was again found to be more effective:

$$l'_{\mathrm{T}} = c_1 + c_2 l'^{0.5}_{0,\mathrm{T}} + c_3 l'_{0,\mathrm{T}} + c_4 l'^{1.5}_{0,\mathrm{T}} + c_5 l'^2_{0,\mathrm{T}} \tag{26}$$

The set of coefficients $c_1, \ldots, c_5$ is obtained by inverting the Vandermonde matrices for the direct problem and the inverse search, Eq. 27 and 28, respectively:

$$\begin{pmatrix} c_1 \\ c_2 \\ c_3 \\ c_4 \\ c_5 \end{pmatrix} = \begin{pmatrix} 1 & l'_{\mathrm{T,min}} & l'^2_{\mathrm{T,min}} & l'^3_{\mathrm{T,min}} & l'^4_{\mathrm{T,min}} \\ 1 & l'_{\mathrm{T},1} & l'^2_{\mathrm{T},1} & l'^3_{\mathrm{T},1} & l'^4_{\mathrm{T},1} \\ 1 & l'_{\mathrm{T,int}} & l'^2_{\mathrm{T,int}} & l'^3_{\mathrm{T,int}} & l'^4_{\mathrm{T,int}} \\ 1 & l'_{\mathrm{T},3} & l'^2_{\mathrm{T},3} & l'^3_{\mathrm{T},3} & l'^4_{\mathrm{T},3} \\ 1 & l'_{\mathrm{T,max}} & l'^2_{\mathrm{T,max}} & l'^3_{\mathrm{T,max}} & l'^4_{\mathrm{T,max}} \end{pmatrix}^{-1} \begin{pmatrix} \gamma'_{\min} \\ \gamma'_{1} \\ \gamma'_{\mathrm{int}} \\ \gamma'_{3} \\ \gamma'_{\max} \end{pmatrix} \tag{27}$$

$$\begin{pmatrix} c_1 \\ c_2 \\ c_3 \\ c_4 \\ c_5 \end{pmatrix} = \begin{pmatrix} 1 & \gamma_{\min}^{0.5} & \gamma_{\min} & \gamma_{\min}^{1.5} & \gamma_{\min}^{2} \\ 1 & \gamma_{1}^{0.5} & \gamma_{1} & \gamma_{1}^{1.5} & \gamma_{1}^{2} \\ 1 & \gamma_{\text{int}}^{0.5} & \gamma_{\text{int}} & \gamma_{\text{int}}^{1.5} & \gamma_{\text{int}}^{2} \\ 1 & \gamma_{3}^{0.5} & \gamma_{3} & \gamma_{3}^{1.5} & \gamma_{3}^{2} \\ 1 & \gamma_{\max}^{0.5} & \gamma_{\max} & \gamma_{\max}^{1.5} & \gamma_{\max}^{2} \end{pmatrix}^{-1} \begin{pmatrix} l'_{\text{T,min}} \\ l'_{\text{T,1}} \\ l'_{\text{T,int}} \\ l'_{\text{T,3}} \\ l'_{\text{T,max}} \end{pmatrix} \tag{28}$$

The use of these higher order polynomials is shown in Fig. 6 for accurate modelling, although more coefficients are required.

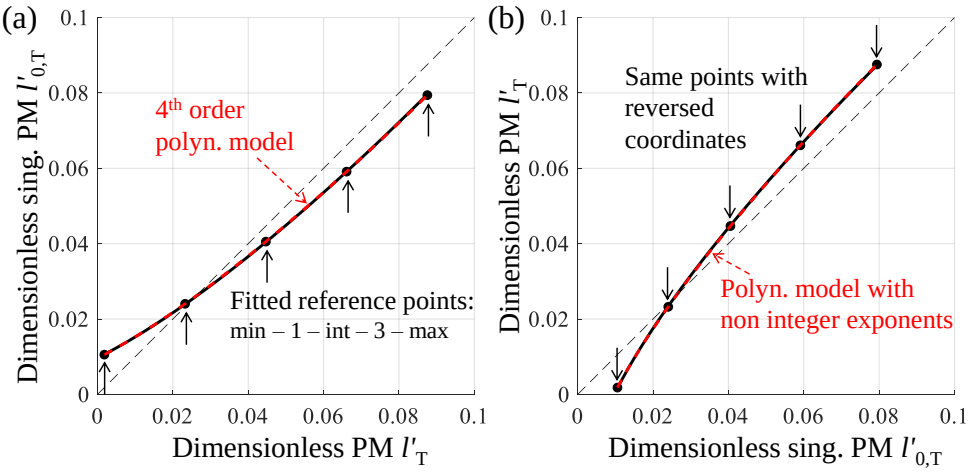

Figure 6: Point Method (a) direct problem and (b) inverse search for $\rho = 0.1$ and $\bar{\alpha} = 60°$.

The relationship between the singularity based and the actual critical distances, for both LM and PM, remains close to the dashed line 1:1 in Figs. 5 and 6, or even coincident for the PM at a specific length value. The two lengths are in fact quite similar if the dimensionless critical distance itself is large. On the other hand, when the critical distance is small, the ratio between these two lengths is quite different from unity.

4. Statistical properties of the critical distance l_T

4.1. The skew-normal distribution

This section focuses on the statistical distribution of the mode III critical distance as obtained according to the LM. The fatigue properties, namely the plain and the notched specimen fatigue strengths, are assumed here to be stochastic variables, and in turn the length l_T is therefore a variable with a probability distribution, which is the target of this analysis. We adopt the same mathematical formalism used to infer the statistical properties of mode I critical length L and SED control radius R_1, see [29, 59]. Input fatigue properties $\Delta\tau_{\text{fl}}$ and $\Delta\tau_{\text{N,fl}}$ are assumed to be normal (Gaussian) random variables, with mean value and standard deviation denoted as $\Delta\bar{\tau}_{\text{fl}}, S, \Delta\bar{\tau}_{\text{N,fl}}, S_{\text{N}}$, respectively. The reasonability and advantages of this option have been already discussed in

[29, 59]. The corresponding coefficients of variation (CV) are defined as follows:

$$r = \frac{S}{\Delta\bar{\tau}_{\mathrm{fl}}}; \quad r_{\mathrm{N}} = \frac{S_{\mathrm{N}}}{\Delta\bar{\tau}_{\mathrm{N,fl}}} \tag{29}$$

We denote with $\bar{l}_{\mathrm{T}}$ the critical distance evaluated, considering the mean values of the plain and the notch fatigue strengths, not necessarily coincident with its mean μ, as shown in the following.

Monte Carlo (MC) simulations (see [29, 59] for more details) highlight interesting properties of the statical distribution of l_{T}. As shown in Fig. 7 for the simplifying case $r_{\mathrm{N}} = r$, the probability density function (PDF) is unimodal with a longer right-side tail.

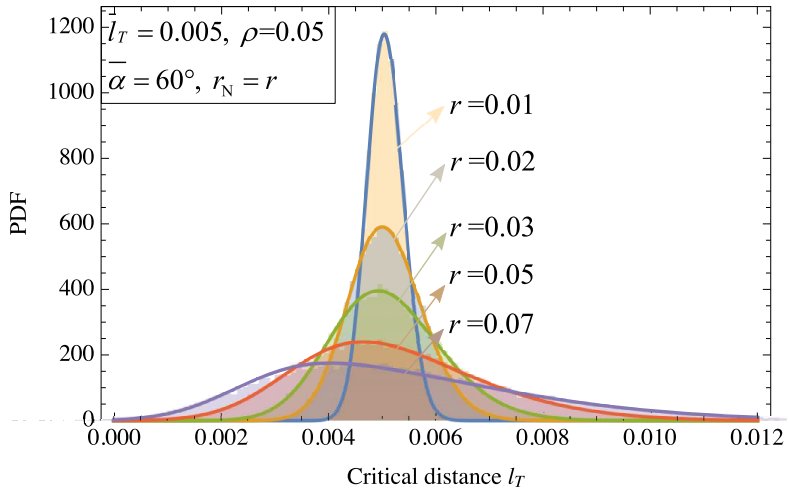

Figure 7: Probability density function (PDF) of critical distance estimations l_{T}. Histograms are obtained from Monte Carlo (MC) simulations. Mean, standard deviation and skewness calculated from MC simulations are used to evaluate the parameters of the skew-normal distributions plotted as solid lines. r is the coefficient of variation (CV) of the plain fatigue limit, which is assumed here to be equal to CV of the notch fatigue limit (r_{N}).

The width at half maximum and the asymmetry degree (i.e. the skewness, positive in the case of a longer right tail) increase with increasing CV r. The PDF histograms shown in Fig. 7 and obtained from l_{T} populations generated via MC are well represented (solid lines) by a tri-parametric skew-normal distribution (SND) as long as r is sufficiently small (not higher than 0.07 in the present work). Its PDF is expressed as follows:

$$PDF(x) = \frac{1}{\sqrt{2\pi}\gamma}\left(1 + \mathrm{erf}\left(\frac{\alpha(x-\beta)}{\sqrt{2}\gamma}\right)\right)\exp\left(-\frac{(x-\beta)^2}{2\gamma^2}\right) \tag{30}$$

Mean μ, standard deviation δ and skewness sk of SND are simple algebraic functions of shape α, location β and scale γ parameters:

$$\mu = \beta + \frac{\sqrt{\frac{2}{\pi}}\alpha\gamma}{\sqrt{1+\alpha^2}} \tag{31}$$

$$\delta = \gamma\sqrt{1 - \frac{2\alpha^2}{\pi(1+\alpha^2)}} \tag{32}$$

Table 5: a_i fit model coefficients for Eq. 34

a_1	a_2	a_3	a_4
2.6159	1.7983	−5.4302	4.1124

$$sk = \frac{\sqrt{2}(4-\pi)\alpha^3}{(\pi+(\pi-2)\alpha^2)^{3/2}} \tag{33}$$

The skewness sk is a function of the only shape parameter α and zeroes for vanishing α. In this case, the SND becomes normal with mean β and standard deviation γ. sk increases monotonically with α and is bounded in the interval (-1,1). Therefore, the SND only reproduces PDF with low-to-moderate sk values. The following analyses are restricted to r values not exceeding 0.07, as it was found that below this threshold value of skewness of l_T, PDF is lower than 1 and therefore the PDF can be represented in the form of SND. The inversion of Eq. 33 to get the shape parameter α from sk is algebraically very challenging. Therefore, the following approximate numerical expression proposed in [29] was implemented:

$$\alpha = \frac{1}{\sqrt{1-sk^2}} \sum_{i=1}^{4} a_i \, sk^{i/2}; \quad 0 \leq sk \leq 1 \tag{34}$$

whose best-fit coefficients a_i are listed in Table 5. Once α has been calculated from Eq. 34, β and γ can be simply evaluated from Eqs. 31, 32.

As discussed by the authors in Refs. [29, 59], the above analyses can be extended to common situations where the two CVs, r and r_N, are different. Exploiting statistical analyses on the distribution of the ratio of normal variables with a low CV [60], the PDF of l_T derived from fatigue properties of not equal r and r_N is almost identical to that obtained under assumption of $r = r_N$, provided that both input fatigue properties have the following equivalent CV:

$$\Sigma = \sqrt{\frac{r^2 + r_N^2}{2}} = r\sqrt{\frac{1+\kappa^2}{2}} \tag{35}$$

Where κ is the CV ratio

$$\kappa = \frac{r_N}{r} \tag{36}$$

The possibility of applying the statistics of l_T inverse search from input fatigue properties of different CV to that obtained assuming $r = r_N = \Sigma$ is confirmed by Fig. 8 (a) and (b), which compares the actual and equivalent (approximated) PDFs of l_T in the lower and upper bound of the proposed validity range of the index κ: $0.5 \leq \kappa \leq 2.2$. Interestingly, the agreement in CV between the two distributions is good, as the relative absolute difference is below 2.5%. It is thus possible to deduce the CV of l_T directly from only the knowledge of Σ. Figure 8 (a) and (b) highlights that the two distributions differ in mean and skewness. Correction functions are

Table 6: Best-fit coefficients of the equations used to estimate NCV of l_T (Eq. 37c)

$\bar{\alpha}$	ν_0	n_1	n_2	n_3	n_4
60°	3.530	−0.92133	0.34992	−0.045173	112.89
90°	4.250	0.97312	0.17790	0.25967	961.51

proposed in the following to adjust these discrepancies.

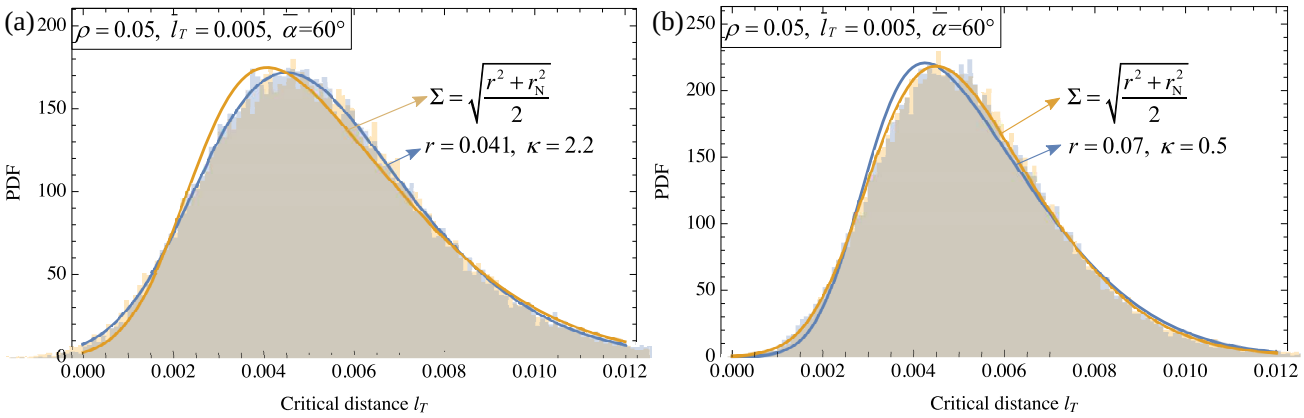

Figure 8: Probability density functions (PDF) of critical distance estimations. The PDF accounting for the effective CV, r and r_N, is compared with that obtained considering, for the plain and notch fatigue limit, the same equivalent CV, namely Σ. (a) is obtained for the maximum, (b) the minimum value of the validity range established for κ.

4.2. Parameters of the skew-normal distribution of l_T

Parametric MC runs were launched to infer the dependency of the mean μ, the length CV δ/μ and the skewness *sk* of l_T on the statistical features Σ and κ of the input fatigue data and the characteristic sizes $\bar{\alpha}$ and ρ of the optimized notched specimen. Since the length CV δ/μ was found in [29, 59] to increase linearly with Σ, it is convenient to normalize it with respect to Σ:

$$\nu = \frac{1}{\Sigma}\frac{\delta}{\mu}; \quad \nu_0(\bar{\alpha}) \leq \nu \leq 7 \Rightarrow \bar{l}_T = \bar{l}_{T,\min} \tag{37a}$$

The resulting normalized CV (NCV) ν is therefore only a function of the specimen geometrical parameters $\bar{\alpha}$ and ρ. As shown in Fig. 9 (a), ν decreases with increasing l_T to ρ ratio and is bounded from below by the condition of infinitely sharp notch ($\rho = 0$, black dashed line in Fig. 9 (a)), which enables ν to be minimized since this geometrical condition results in the steepest notch stress gradient. This lower bound of NCV will be denoted as ν_0 and is listed in Table 6 for the two explored $\bar{\alpha}$ angles. Clearly, the use of radiused notches results in l_T estimates affected by larger ν. The higher the notch radius to critical distance ratio ρ/l_T, the larger the resulting ν value.

To eliminate the explicit dependency of the statistical properties of l_T upon the notch radius ratio ρ, we follow the same approach as in [29, 59]. We investigate the statistics of the inverse search of l_T performed using a notched specimen of notch radius ratio ρ resulting in a fixed predetermined value of ν. To determine this locus

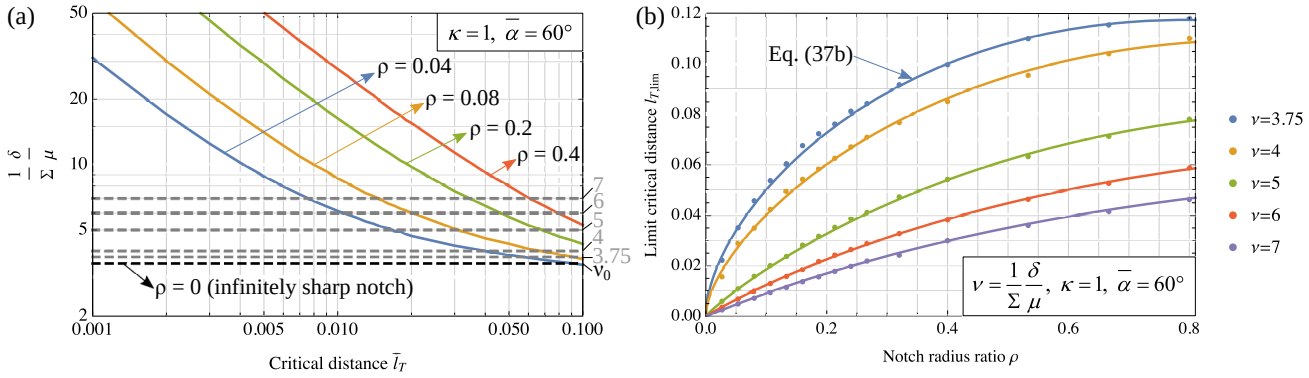

Figure 9: (a) The CV of l_T estimations normalized to Σ (and denoted as ν) depends on the notch radius ratio ρ. Here, the statistical properties of l_T are evaluated considering discrete values of ν, ranging from ν_0 (corresponding to an infinitely sharp notch, black dashed line) to 7. (b) $l_{T,lim}$ is the locus of critical distances for varying notch radii ρ corresponding to a certain value of ν.

Table 7: Best fit coefficients of the equations used to estimate $l_{T,min}$ (Eq. 37b)

$\bar{\alpha}$	ν	b_1	b_2	b_3
60°	3.75	0.12361	0.16617	−0.17603
	4	0.086041	0.17797	−0.15480
	5	0.0041091	0.21648	−0.13899
	6	−0.00045055	0.15402	−0.090108
	7	−0.0034339	0.12326	−0.068260
90°	4.5	0.096206	0.052678	−0.052898
	5	0.038808	0.12664	−0.082560
	6	0.0066008	0.12503	−0.068673
	7	0.0029409	0.087041	−0.039904

of l_T, the intersections of the curves parametrically plotted in Fig. 9 (a) need to be searched for with the equation $\nu = \text{const}$. We consider a discrete set of constant ν values (represented by grey dashed lines in Fig. 9 (a)), namely 3.75,4,5,6,7 and 4.5,5,6,7 for $\bar{\alpha} = 60°$ and $\bar{\alpha} = 90°$, respectively. The dotted values in Fig. 9 (b) represent the numerically computed roots of this nonlinear system of equations solved parametrically for such discrete set of ν values. They are well represented by the following algebraic expression:

$$l_{T,lim} = b_1(\bar{\alpha},\nu)\rho^{1/2} + b_2(\bar{\alpha},\nu)\rho + b_3(\bar{\alpha},\nu)\rho^{3/2} \tag{37b}$$

whose best-fit coefficients are listed in Table 7.

In other words, Eq. 37b identifies the locus of l_T characterized by a fixed NCV. Interestingly, Eq. 37b can be inverted (analytical expression not reported here for the sake of brevity) to determine the locus of notch radii ρ_{lim} which leads to a l_T estimation affected by a given NCV ν. The dotted values in Fig. 10 are the roots of the inverted Eq. 37b parametrically calculated for the discrete set of ν values. Of note, these points show a trend converging to ν_0 for vanishing ρ (infinitely sharp notch) which is well represented by the following expression

(solid lines in Fig. 10):

$$\nu = \nu_0(\bar{\alpha}) + \frac{n_1(\bar{\alpha})\sqrt{\rho} + n_2(\bar{\alpha})\dfrac{\rho}{\bar{l}_\mathrm{T}} + n_3(\bar{\alpha})\dfrac{\rho^2}{\bar{l}_\mathrm{T}}}{1 + n_4(\bar{\alpha})\bar{l}_\mathrm{T}^2} \tag{37c}$$

whose best-fit coefficients n_i are listed in Table 6. Importantly, Eq. 37c enables the notch radius of the notched specimen to be designed according to the expected critical length l_T and the desired level of NCV ν. In addition, given the notch radius ratio ρ, the NCV ν of l_T can be calculated.

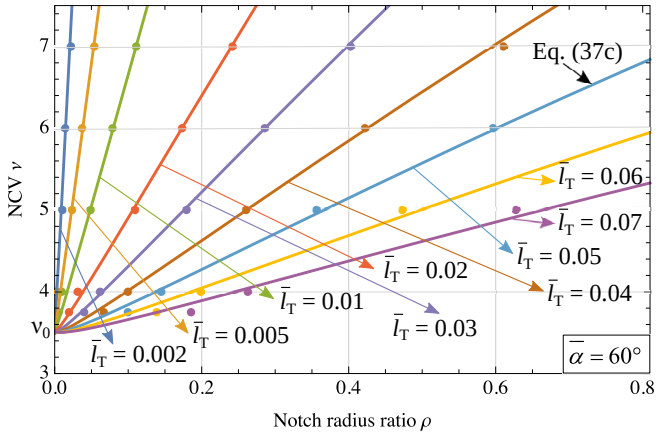

Figure 10: The dependency of ν on ρ and $\bar{l}_\mathrm{T}$ is well represented by Eq. 37c.

Knowledge of ν in turn enables the statistical properties of l_T to be deduced. Accordingly, the length CV can be readily evaluated from Eq. 37a. Figure 11 illustrates the results of MC simulations keeping ν fixed (at 5 in this case) and adjusting the value of $\bar{l}_\mathrm{T}$ according to Eq. 37b. NCV falls within a relative error band across ν, comprised of between -1.0% and 2.5%, irrespectively of the statistical properties Σ and κ (Fig. 11 (b)) of the input fatigue data and of the notch radius ratio ρ (Fig. 11 (a)). This result confirms the ability of Eqs. 35 and 37a to bring the NCV of l_T for a generic set of input fatigue data back to that predicted for $\kappa = 1$ ($r = r_\mathrm{N}$).

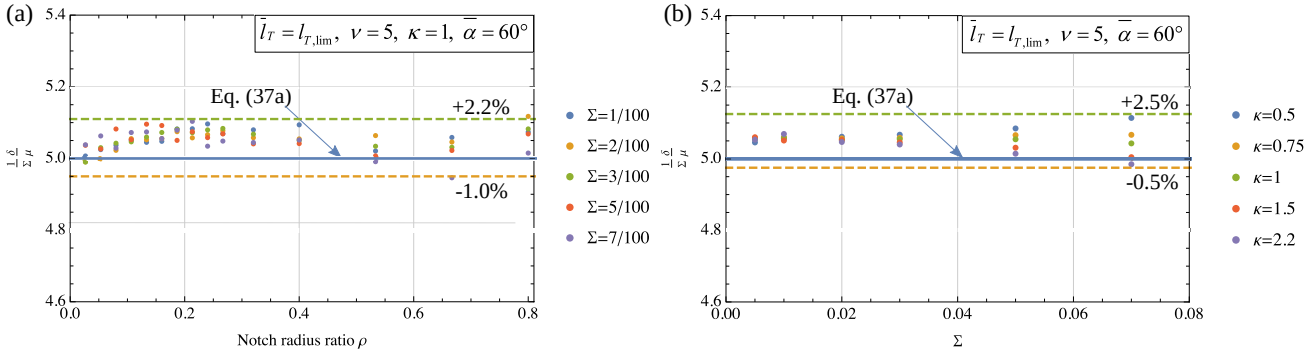

Figure 11: The NCV ν for the locus $l_{\mathrm{T,lim}}$ is fairly independent (a) of Σ and ρ within an error band 1.0%, 2.2% and of (b) Σ and κ within an error band 0.5%, 2.5%.

In the following, MC simulations are used to derive suitable expressions to predict mean and skewness of l_T. They are carried out parametrically for the discrete ν values. Simple interpolation can be used to evaluate the

two statistical properties for any intermediate ν value assessed via Eq. 37c.

Figure 12 (a) and (b) plot the mean value μ normalized to $\bar{l}_T$ as a function of ρ and Σ for $\kappa = 0.5$ and $\kappa = 2.2$, respectively. Unlike mode I critical length and SED control radius, the mean μ is also a (declining) function of the notch radius ratio ρ. For this purpose, the following tri-variate interpolating function is proposed here to fit the dotted values corresponding to the MC experiments:

$$\frac{\mu}{\bar{l}_T} = m_1(\bar{\alpha},\nu) + \frac{m_2(\bar{\alpha},\nu)\,\Sigma^2}{\left(1+m_3(\bar{\alpha},\nu)\sqrt{\kappa}\right)\left(1+m_4(\bar{\alpha},\nu)\left(\frac{a}{2}\rho\right)^{m_5(\bar{\alpha},\nu)}\right)} \tag{37d}$$

whose best-fit coefficients m_i are listed in Table 8.

Table 8: Best fit coefficients of the equation used to estimate the mean value over $\bar{l}_T$ ratio (Eq. 37d).

$\bar{\alpha}$	ν	m_1	m_2	m_3	m_4	m_5
60°	3.53	1	22.372	2.4604	1	1
	3.75	1.0022	2041.9	253.53	2.2485	0.27106
	4	1.0018	2988.7	154.73	5.5349	0.17527
	5	0.99902	128.72	6.3145	10.779	0.52899
	6	0.99659	81.239	3.9468	24.290	0.90911
	7	0.99506	81.937	3.4280	41.579	1.1062
90°	4.25	1	23.501	1.5503	1	1
	4.5	1.0027	100.14	10.916	2.0083	0.48512
	5	1.0010	103.84	5.3844	3.5556	0.30453
	6	0.99713	77.771	3.0126	8.3191	0.59270
	7	0.99394	74.570	2.5711	19.284	0.91296

Figure 12 shows that, despite the complicated trend highlighted by the dotted values, Eq. 37d (solid lines) fits the MC experiments fairly well, and the absolute relative error is kept below 1%.

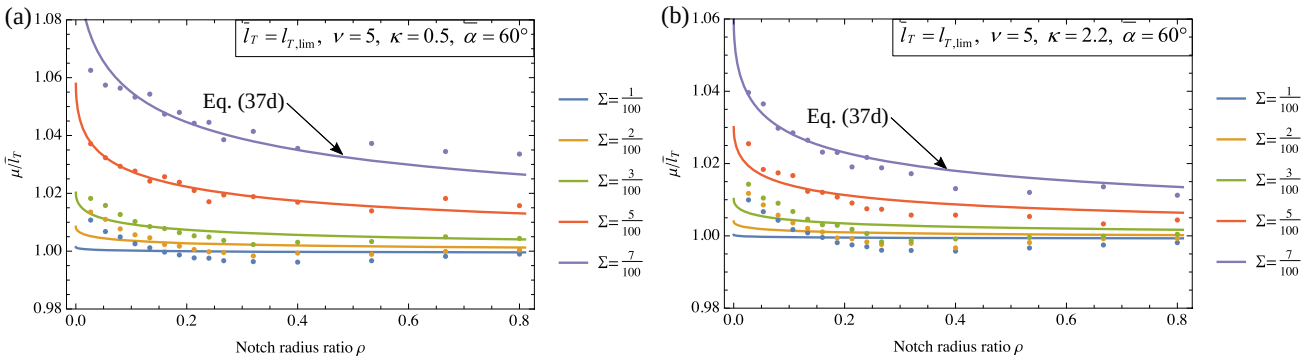

Figure 12: The mean normalized to the input length $\bar{l}_T$ (estimated from the mean of plain and notch fatigue limits) is a function of the notch radius ratio ρ and input fatigue data statistical properties Σ and κ. These dependencies are satisfactorily predicted by Eq. 37d. (a) and (b) refer to the lower and upper bound of the explored values of κ, viz. 0.5 and 2.2, respectively. Dotted values are the results of MC simulations, affected by some statistical fluctuations.

Figure 13 (a) and (b) plot the skewness *sk* as a function of ρ and Σ for $\kappa = 0.5$ and $\kappa = 2.2$, respectively. Also in this case, the MC experiments denote a dependency not only on Σ and κ, but also on ρ. The following tri-variate

function is then proposed to interpolate the data:

$$sk = \frac{s_1(\bar{\alpha},\nu)\,\Sigma + s_2(\bar{\alpha},\nu)\,\Sigma^2}{\left(1+s_3(\bar{\alpha},\nu)\sqrt{\kappa}\right)\left(1+s_4(\bar{\alpha},\nu)\left(\frac{a}{2}\rho\right)^{s_5(\bar{\alpha},\nu)\kappa+s_6(\bar{\alpha},\nu)}\right)} \tag{37e}$$

whose best-fit coefficients s_i are listed in Table 9.

Table 9: Best fit coefficients of the equation used to estimate the skewness of l_T (Eq. 37e).

$\bar{\alpha}$	n_i	s_1	s_2	s_3	s_4	s_5	s_6
60°	3.53	48.054	79.153	3.7474	1	1	1
	3.75	41.376	24.224	3.1506	40.722	−0.17069	1.4653
	4	46.082	24.175	3.6358	30.582	−0.15974	1.4461
	5	43.751	36.895	3.2785	12.007	−0.14766	1.2711
	6	45.524	47.213	3.4084	6.7841	−0.13678	1.1249
	7	43.092	46.486	3.1245	4.7260	−0.13870	1.0348
90°	4.25	49.292	105.18	3.1122	1	1	1
	4.5	38.045	3.7475	2.2097	43.485	−0.12863	1.4383
	5	41.739	16.599	2.4349	22.804	−0.097834	1.2823
	6	41.840	38.866	2.4053	10.791	−0.093331	1.1418
	7	46.732	49.577	2.7341	6.4515	−0.067528	0.98986

The solid lines in Fig. 13 indicate that the Eq. 37e well represents the MC experiments with absolute relative errors below 5%. In conclusion, Table 10 summarizes the validity range of the proposed method to deduce the statistical properties of the inverse estimations of the critical distance l_T.

This statistical procedure, as well as the previous procedure for the initial determination of the mode III critical distance, are implemented in two MATLAB scripts, which are in the electronic version of the paper and described below in the Appendix.

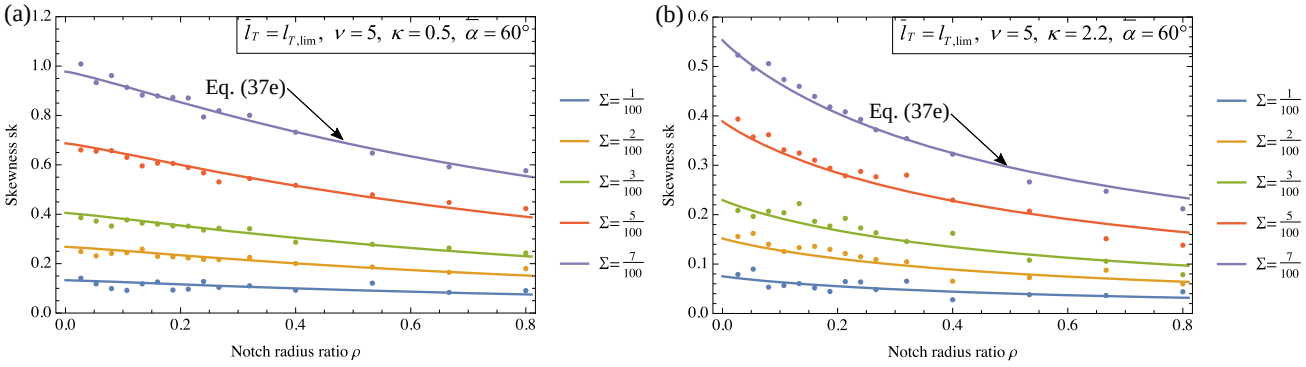

Figure 13: The skewness sk is a function of the notch radius ratio and input fatigue data statistical properties Σ and κ. These dependencies are satisfactorily predicted by Eq. 37e. (a) and (b) refer to the lower and upper bound of the explored values of κ, viz. 0.5 and 2.2, respectively. Dotted values are the results of MC simulations, affected by some statistical fluctuations.

Table 10: Requirements for statistically validated l_T estimations.

Requirements on input fatigue data	Requirements on l_T inverse search
$\Sigma \leq 0.07$	$l_{T,min} \leq \bar{l}_T \leq l_{T,max}$
$0.5 \leq \kappa \leq 2.2$	$\nu = \nu(\bar{l}_T, \rho) \Rightarrow \nu \leq 7$

5. Example of the implementation

5.1. Experimental data

To test the inverse search procedure of the critical length and its statistical properties, an experimental campaign was carried out on specimens extracted from bars of 42CrMo4+QT (quenched and tempered) steel. The fatigue characterization was carried out under fully-reversed (load ratio $R = -1$) torsional fatigue on an axisymmetric plain and V-notched samples, whose geometries are shown in Fig. 14. The sharp notch was turned using a cutting tool insert with corner radius of 0.1 mm. The actual local radius was experimentally verified under stereomicroscopy inspections (shown in the figure) and evaluated to be $R = 0.157 \pm 0.007$ mm.

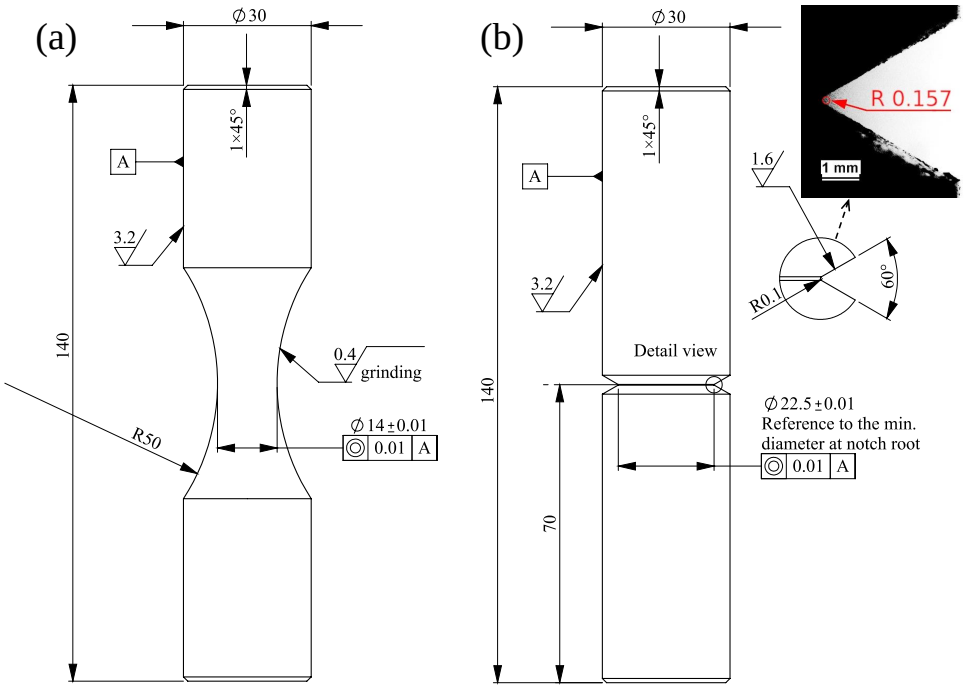

Figure 14: Technical drawings of (a) plain specimen and (b) optimized notched specimen, with opening angle $\bar{\alpha} = 60°$ and detection of the actual notch radius (lengths in mm).

The fatigue tests were conducted in laboratory environment using a biaxial servo-hydraulic testing machine Walter+Bai (Löhningen, Switzerland) LFV100-T1000-HH equipped with a biaxial load cell with 100 kN and 1000 Nm axial and torsional load capacity, respectively. The load control imposed a sinusoidal torsional load waveform with frequency of 20 Hz. The medium-to-high-cycle fatigue life in the range between nearly 5×10^4 and 5×10^6 cycles was explored employing 12 plain or notched specimens. The fatigue curves corresponding to

50% failure probability, represented by Basquin's equation:

$$\tau_{\mathrm{a}} = k_1 N_{\mathrm{f}}^{k_2} \tag{38}$$

were determined by fitting the $\log(N_{\mathrm{f}})$ versus $\log(\tau_{\mathrm{a}})$ results. The scatter of the fatigue data was assessed by computing the estimated regression variance which was assumed to be uniform for the entire fatigue life range, and expressed by:

$$S^2 = \frac{\sum_{i=1}^{q} (\tau_{\mathrm{a},i} - \hat{\tau}_{\mathrm{a},i})^2}{q - p} \tag{39}$$

where $\tau_{\mathrm{a},i}$ is the i-th fatigue amplitude data point, $\hat{\tau}_{\mathrm{a},i}$ is its estimator, q is the number of data elements, and p is the number of parameters in the regression (p = 2 in the present case). The S-N data are reported in Fig. 15 along with the fit curves (with 50%, solid line, and 10% and 90%, dashed lines, failure probability). The high cycle fatigue strength computed at 5×10^6 cycles and the corresponding standard deviation are reported in Table 11.

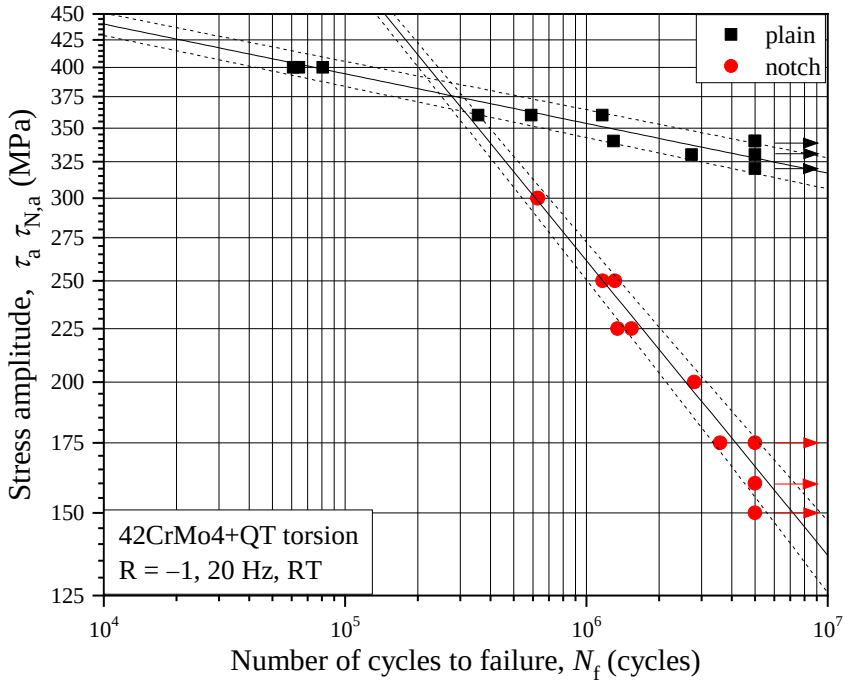

Figure 15: S-N curves of plain and notched specimens used for the inverse search estimation of l_{T}. Solid lines refer to 50% failure probability, dashed lines to 10% and 90% failure probabilities.

Table 11: Torsion fatigue strength characteristics of the investigated specimen geometries made of steel 42CrMo4+QT.

Material	R	Geometry	k_1 (MPa)	k_2	Fatigue life (cycles)	$\Delta\bar{\tau}_{\mathrm{fl}}$, $\Delta\bar{\tau}_{\mathrm{N,fl}}$ (MPa)	S, S_{N} (MPa)	CV r, r_{N}
42CrMo4+QT	−1	Plain	681.6	−0.048	5×10^6	327.5	8.46	0.026
		Notched	12863	−0.282	5×10^6	165.7	8.45	0.051

5.2. Inverse search and statistical distribution of L_T

The results of the inverse search for L_T, from the experimental data just introduced, are listed in Table 12. More precisely, $\bar{L}_T$ was obtained after iteratively applying the inverse search procedure, and considering the relative size of $\bar{L}_T$ itself with respect to the plain specimen radius. The fatigue stress concentration factor was initially determined referring to the nominal stress τ_N, Fig. 1, leading to:

$$K_{fT} = \frac{327.5}{165.7} = 1.976 \rightarrow \bar{L}_T = 0.226 \text{ mm} \tag{40}$$

Now the gradient stress of the plain specimen itself can be averaged over the length $2\bar{L}_T$, and having a linear distribution, this average is equivalent to the evaluation at $\bar{L}_T$:

$$\tau_{N,1} = \tau_N \frac{d/2 - \bar{L}_T}{d/2} = 322.2 \text{ MPa} \tag{41}$$

which is slightly lower than τ_N and $d = 14$ mm is the diameter of the plain specimen, Fig. 14.
After this nominal stress correction $\tau_{N,1}$, the value of K_{fT} can be updated. A lower result is obviously obtained, leading to a slightly higher critical distance. This procedure can be easily iterated, and a quite stable combination of corrected nominal shear stress and critical distance is obtained after a few steps:

$$\tau_{N,4} = 315.7 \text{ MPa} \rightarrow K_{fT} = 1.905 \rightarrow \bar{L}_T = 0.252 \tag{42}$$

The same iterative correction can also be performed with the PM, for which the stress was required to be evaluated at $\bar{L}'_T/2$. The not corrected K_{fT} produced:

$$K_{fT} = \frac{327.5}{165.7} = 1.976 \rightarrow \bar{L}'_T = 0.348 \text{ mm} \tag{43}$$

and after a few interactions, the following stable result was obtained:

$$K_{fT} = 1.924 \rightarrow \bar{L}'_T = 0.373 \text{ mm} \tag{44}$$

The statistical properties of the LM length are reported in Table 12 and were estimated using both Eqs. 37a – 37e and MC simulations where, during each trial, L_T was computed by extracting the normally distributed values of plain and notch fatigue strengths. The agreement between the statistical properties estimated in these two ways is convincing, as the absolute relative error is below 3%.

Table 12: Statistical properties of l_T obtained for steel 42CrMo4+QT.

$\bar{L}_T$ (mm)	$\bar{L}'_T$ (mm)	Σ	κ	ν	Monte Carlo			Eqs. 37a – 37e		
					$\mu/\bar{l}_T$	δ/μ	sk	$\mu/\bar{l}_T$	δ/μ	sk
0.252	0.373	0.0405	1.976	4.188	1.011	0.169	0.291	1.009	0.169	0.291

Figure 16 compares the PDF of L_T estimated through MC simulations (histogram) and the SND with parameters deduced from Eqs. 37a – 37e. Once again, the agreement between the two approaches is very good.

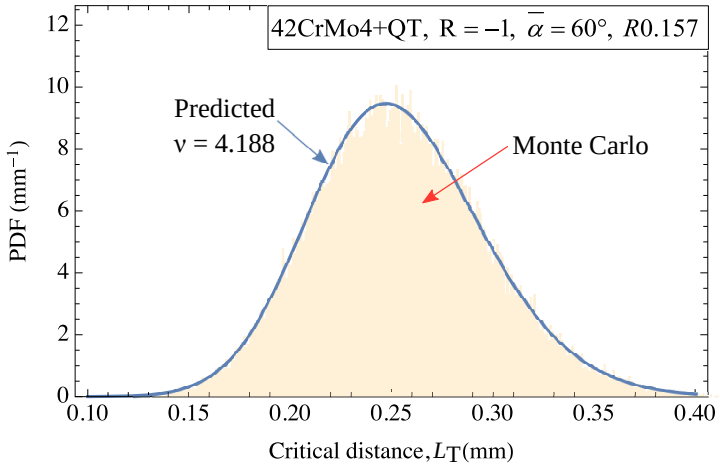

Figure 16: Comparison between PDF estimated through MC simulations and predicted by Eqs. 37a – 37e.

A large L_T was found compared to the mode I critical distance L, and as mentioned in the Introduction, this situation is usual for steels. The ratio between the L of the same steel, reported in Ref. [27], and the L_T obtained here, is in the order of 0.1. The ratios reported in Refs. [20, 46] for similar steel, were also below 0.5. Berto et al. [34] again found limited ratios, even smaller than 0.1, referring to the control radii R_1 and R_3 for the SED criterion. Further investigations are planned regarding the large discrepancy between these two lengths, extending the analysis to other materials with a different ductility and thus a different fatigue limit over yield strength ratio.

6. Size effect of the specimens on the critical distance determination

The critical distance can be effectively determined when a limited uncertainty of the inverse search is attributed to the result, or in other words when the critical distance standard deviation is small. However, the fatigue input strength values are also affected by a probability distribution which can be considered an extrinsic effect, attributed to the material, thus not dependent on the specimen geometry itself. A good estimator is therefore provided by the NCV ν, introduced above, which is a measure of the standard deviation, however, normalized in terms of the (combined and relative) standard deviation Σ of the fatigue strength input. From Eq. 37c, ν depends on the notch angle $\bar{\alpha}$, the notch radius ratio ρ, and also importantly on the critical distance itself $\bar{l}_T$. The best situation for the inverse search is when the critical distance, or more precisely a length equal to twice the critical distance, according to the LM criterion, lies in a strong gradient region. This condition is obtained when the angle is quite sharp, though an angle smaller than 60° is difficult to obtain in terms of manufacturing, and most importantly, with a small notch radius. In principle, an almost perfectly sharp notch is

desirable, however, again from a manufacturing perspective, the real notch radius cannot be smaller than 0.2 mm with common manufacturing tools, or 0.1 mm at most. In addition, this radius needs to be known with accuracy, for example measured using a section and microscope observation or with an optical profile identification. In the example presented here, the notch radius detected was $R = 0.157$ mm, as shown in Fig. 14, despite the nominal value of 0.1 mm. Additional tests were performed to determine the mode I length with the same notch angle and same nominal notch radius, which are not reported here for the sake of brevity, and the actual (measured) radius was 0.12 mm. The length $L = 0.027$ mm was obtained, in perfect agreement with our previous result [27].

As shown in Fig. 17, a notch radius as small as the mode I critical distance is not possible for common high strength metal alloys. However, at least an intermediate radius between the two mode I and mode III lengths is recommended, whereas a blunt notch is obviously not.

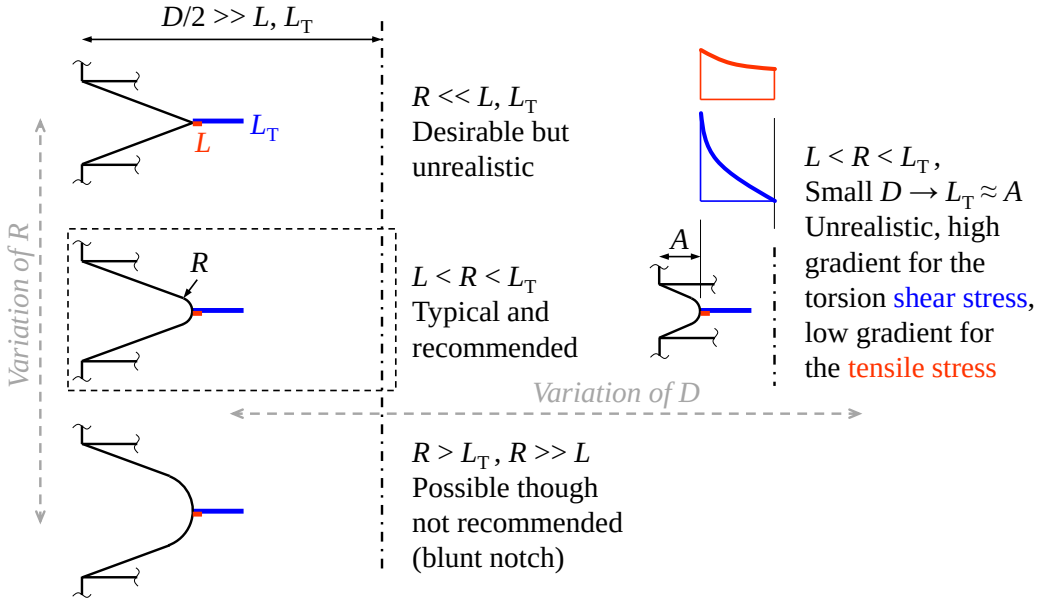

Figure 17: Different possible relative size combinations between mode I and mode III lengths, specimen outer diameter and notch radius, and recommended setup for an optimal inverse search determination of the critical distances.

In addition to the notch radius, which is the main geometry parameter, the outer diameter of the specimen D also plays a role. This length cannot be either too large or too small for practical reasons, however, some considerations are of interest even in the common range of this dimension. If the diameter is very large, the stress gradient is basically just driven by the notch radius for both mode I and mode III. On the other hand, if small or even very small values of D are considered, although perhaps unrealistic, the effect of this parameter is different between the two loading modes. The torsional loading involves a nominal stress gradient which obviously is enhanced by a small D, and this synergically interacts with the notch induced stress concentration. For this reason, the mode III NCV is lower for a smaller D, while for mode I, the stress gradient in a region equal to $2L$ (according to the LM) is less severe. Thus in turn, the mode I NCV increases with smaller D values, which as previously

discussed, are not recommended.

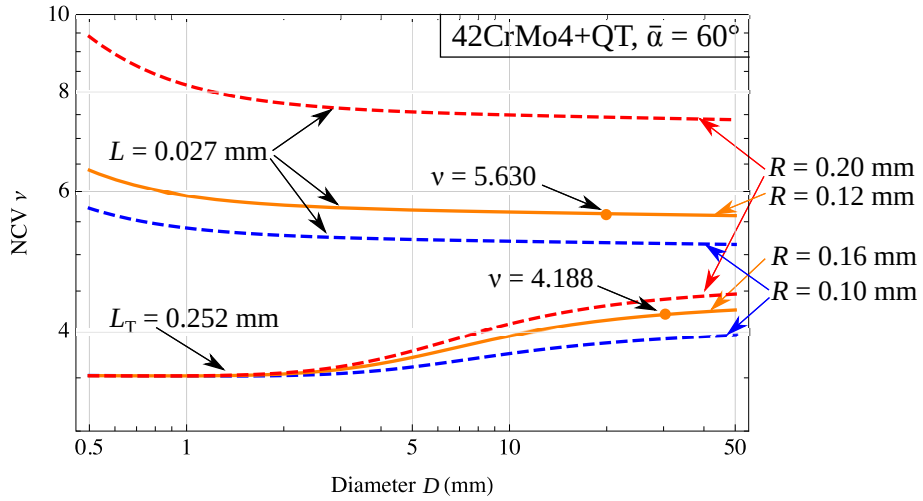

Figure 18: Parametric analysis of the effect induced by the outer diameter of the specimen and the notch radius, on the inverse search NCV, for mode I and III critical distances. Experimental configurations and the values obtained for the 42CrMo4+QT steel are reported as references.

These trends are summarized in Fig. 18. The dimensions of the actual specimens presented above, determined $\nu = 5.630$ and $\nu = 4.188$ for mode I and mode III, respectively. Although not experimentally investigated, other hypothetical diameter and notch radius values are presented in this figure together with the related effects on ν. The same lengths L and L_T are maintained, which are considered as pure material properties, not affected by the geometry and the size. The figure highlights that NCV decreases for mode I, but increases for mode III, with respect to the diameter D. The mode I NCV values are notably higher than for mode III, which is mainly due to the relative size of the critical distance with respect to the notch radius. As L_T is quite large, even larger than the notch radius, the relative gradient on the averaging length is higher, which implies a more stable inversion as previously highlighted. Different notch radii are analysed in this investigation: the two nominal values 0.1 mm and 0.2 mm, which are the common tool nose radii, and the actual (or detected) sizes of the radius $R = 0.12$ mm and $R = 0.16$ mm for mode I and mode III, respectively. A larger radius sensibility is evident for mode I, again because the L value is smaller than the radius itself. The smallest possible notch radius is thus required, such as $R = 0.1$ mm. On the other hand, this requirement is less demanding for mode III, for which a ν lower than 4.5 can be obtained even with $R = 0.2$ mm.

7. Conclusions

We have presented a procedure to determine the mode III (or torsional) critical distance along with a dedicated V-notched specimen with optimal notch design. The analytical procedure proposed is based on fit functions after accurate and comprehensive finite element simulations, and the use of a dimensionless form, for all the lengths, provided an efficient method for this calculation. Our approach is to initially evaluate the critical distance just

according to the singular term, ideally assuming a perfectly sharp notch. This length is subsequently corrected by introducing the notch radius, and this process is followed both according to the Line and the Point Methods. A statistical analysis is then provided for the Line Method critical distance, by implementing Monte Carlo simulations and again a modelling with dedicated fit functions is proposed. After determining just a single value for the critical distance, its stochastic distribution is thus also provided. Assuming a normal distribution for the two input variables, i.e. the plain and the notched specimen fatigue strengths, a skew-normal distribution is evident for the torsional critical distance, which is in agreement with our previous study on the mode I critical distance.

A normalized coefficient of variation (NCV) for the torsional critical distance standard deviation was defined and modelled. This parameter was considered in this study as an effective indicator to determine the quality of the inverse search critical distance. The NCV was therefore parametrically analysed in terms of the notched specimen dimensions, and for a comparison, the same investigation was concurrently done for the mode I critical distance. A typical quenched and tempered steel was considered as an example, and a significantly larger mode III critical distance was obtained than the mode I. Since a much larger mode III length was obtained, the role of the notch radius ratio in terms of the NCV was found less dominant than for mode I. In other words, for an accurate determination of the mode I critical distance, the smallest possible notch radius is recommended, and an accurate measure is required. On the other hand, for the (larger) mode III length, this focus on the radius is less important. The size effect of the outer diameter is also worth investigating, and again a countertrend was obtained between the two mode lengths. A large diameter is desirable for mode I, while the inherent gradient of the torsional stress distribution suggests a small diameter to determine the mode III length.

Future developments of the present work will include the effect of plasticity and orientation of the early crack propagation plane with respect to the specimen symmetry plane, considering a wide spectrum of structural metallic materials.

Acknowledgements

This project was supported by the Italian Ministry of Education, University, and Research (MIUR) within the program “Departments of Excellence” 2018–2022 (DII-UNITN)

Appendix A. Software implementation

This appendix describes the use of editable MATLAB scripts, available with the online version of this paper, for a rapid implementation of the two proposed procedures.

The script `LM_PM_ExampleModeIII.m` describes the inverse search determination of the mode III critical

distances according to both the Line and Point Methods. The input data derive from the experimental example previously presented:

$$\begin{aligned} &\bar{\alpha} = 60^\circ \\ &D = 30 \text{ mm} \\ &R = 0.157 \text{ mm} \\ &K_{\text{fT}} = 1.905 \end{aligned} \tag{A.1}$$

After selecting $\bar{\alpha}$, the coefficients of the procedure are defined from Tables 1, 2, 3, 4. The torsional stress concentration factor can be initially found with Eq. 5:

$$K_{\text{tT}} = 3.706 \tag{A.2}$$

and it is substantially larger than K_{fT}, which correctly implies a positive mode III critical distance.
The singularity based LM length is deduced from the K_{fT} and the N-SIF parameters, Eq. 8, thus obtaining:

$$l_{0,\text{T}} = 0.02051 \tag{A.3}$$

The minimum and maximum (dimensionless) lengths can be found, along with the intermediate length, with Eqs. 13:

$$\begin{aligned} &l_{\text{T,min}} = 0.00082 \\ &l_{\text{T,max}} = 0.06326 \\ &l_{\text{T,int}} = 0.03204 \end{aligned} \tag{A.4}$$

The LM inversion function corresponding values are obtained with Eq. 14:

$$\begin{aligned} &\gamma_{\text{min}} = 0.00462 \\ &\gamma_{\text{int}} = 0.03671 \\ &\gamma_{\text{max}} = 0.07271 \end{aligned} \tag{A.5}$$

The Vandermonde matrices for both the LM direct problem and the inverse search are computed according to Eqs. 17 and 18. The singularity based length $l_{0,\text{T}}$, reported before in Eq. A.3, is then converted into l_{T} with Eq. 16, and finally scaled with $D/2$ to obtain the actual length:

$$L_{\text{T}} = l_{\text{T}}(D/2) = 0.252 \text{ mm} \tag{A.6}$$

In order to obtain a confirmation, the direct problem can be solved, Eq. 15, with an appropriate set of coefficients c_1, c_2, c_3, and by considering the input L_{T} obtained here. The (back-calculated) fatigue stress concentration factor

is thus $K_{\mathrm{fT}} = 1.9028$, in good agreement with the input (experimental) K_{fT} value.

The procedure for the PM, follows very similar steps, although involving larger Vandermonde matrices and five coefficients $c_1, \ldots, c_5$. Although not reported here for the sake of brevity, all the variables are available by running the MATLAB script file.

The same experimental scenario can be used for the other procedure, to assess the statistical properties of the critical distance, and implemented in the script `LM_StatisticalModeIII.m`. The critical distance is now considered a statistical variable, thus the barred symbols are used, as explained above: $\bar{l}_{\mathrm{T}} = 0.0168, \bar{L}_{\mathrm{T}} = 0.252$ mm. The required coefficients for the procedure can be retrieved in Tables 6, 7, 8 and 9 after the selection of the notch angle $\bar{\alpha}$. The NCV can be calculated according to the dimensionless lengths ρ and $\bar{l}_{\mathrm{T}}$, with Eq. 37c, and the following result is obtained:

$$\nu = 4.188 \tag{A.7}$$

The statistical distribution of the input fatigue strengths of plain and notched specimens can now be considered. The CVs of the two specimens, r and r_{N} are calculated, and thus their κ ratio and the equivalent CV Σ are easily obtained:

$$\begin{aligned} \kappa &= 1.976 \\ \Sigma &= 0.0405 \end{aligned} \tag{A.8}$$

The statistical properties of the skew-normal distribution can now be derived. The mean value is obtained with Eq. 37d. More precisely, this equation is used for the ν values listed in Table 8, and the corresponding $\mu/\bar{l}_{\mathrm{T}}$ ratio values are then interpolated according to the actual $\nu = 4.188$. An accurate mean value is thus obtained:

$$\mu/\bar{l}_{\mathrm{T}} = 1.009 \rightarrow \mu = 0.0170 \tag{A.9}$$

which implies that the mean value of the dimensionless critical distance is slightly larger than the barred, due to the asymmetry of the distribution. The standard deviation δ is then easily obtained by recalling the NCV definition, thus inverting Eq. 37a:

$$\delta = \nu \Sigma \mu = 0.00287 \tag{A.10}$$

The final parameter needed for the complete definition of the distribution is the skewness sk. As above for μ, Eq. 37e is used, however, by evaluating the skewness for the values of ν in Table 9, and then again interpolating for the actual ν, and finally obtaining:

$$sk = 0.291 \tag{A.11}$$

Now the three parameters μ, δ, sk need to be converted into the shape, location and scale parameters, α, β, γ, respectively, to obtain the analytical expression for the PDF. The parameter α is initially deduced with the proposed approximated numerical expression, Eq. 34, just from sk. The parameter γ can be obtained from δ and α, now both available, by inverting Eq. 32. And β is then obtained by inverting Eq. 31, with all the required parameters μ, α and γ available.

$$\begin{aligned} \alpha &= 1.496 \\ \beta &= 0.01441 \\ \gamma &= 0.003840 \end{aligned} \tag{A.12}$$

The parameters α, β and γ are for the dimensionless form of the l_{T} distribution. For the distribution of L_{T}, the variable l_{T} needs to be multiplied by $D/2$, thus the corresponding PDF values need to be divided by $D/2$, and the distribution in shown in Fig. 16 is obtained.

Appendix B. Supplementary material

The following are the supplementary MATLAB files attached to this article:

`LM_PM_ExampleModeIII.m`

`LM_StatisticalModeIII.m`

References

[1] C. Bagni, H. Askes, L. Susmel, Gradient elasticity: a transformative stress analysis tool to design notched components against uniaxial/multiaxial high-cycle fatigue, Fatigue & Fracture of Engineering Materials & Structures 39 (8) (2016) 1012–1029. doi:10.1111/ffe.12447.

[2] N. Gates, A. Fatemi, Notch deformation and stress gradient effects in multiaxial fatigue, Theoretical and Applied Fracture Mechanics 84 (2016) 3–25. doi:10.1016/j.tafmec.2016.02.005.

[3] R. Branco, J. D. Costa, F. Berto, A. Kotousov, F. V. Antunes, Fatigue crack initiation behaviour of notched 34CrNiMo6 steel bars under proportional bending-torsion loading, International Journal of Fatigue 130 (2020) 105268. doi:10.1016/j.ijfatigue.2019.105268.

[4] J. Mei, S. Xing, A. Vasu, J. Chung, R. Desai, P. Dong, The fatigue limit prediction of notched components – A critical review and modified stress gradient based approach, International Journal of Fatigue 135 (2020) 105531. doi:10.1016/j.ijfatigue.2020.105531.

[5] M. Benedetti, V. Fontanari, C. Santus, M. Bandini, Notch fatigue behaviour of shot peened high-strength aluminium alloys: Experiments and predictions using a critical distance method, International Journal of Fatigue 32 (10) (2010) 1600–1611. doi:10.1016/j.ijfatigue.2010.02.012.

[6] M. Benedetti, V. Fontanari, M. Allahkarami, J. C. Hanan, M. Bandini, On the combination of the critical distance theory with a multiaxial fatigue criterion for predicting the fatigue strength of notched and plain shot-peened parts, International Journal of Fatigue 93 (2016) 133–147. doi:10.1016/j.ijfatigue.2016.08.015.

[7] D. Taylor, The Theory of Critical Distances: A New Perspective in Fracture Mechanics, Elsevier Science and Technology, 2007.

[8] D. Taylor, Applications of the theory of critical distances in failure analysis, Engineering Failure Analysis 18 (2) (2011) 543–549. doi:10.1016/j.engfailanal.2010.07.002.

[9] T. Yin, A. Tyas, O. Plekhov, A. Terekhina, L. Susmel, A novel reformulation of the Theory of Critical Distances to design notched metals against dynamic loading, Materials and Design 69 (2015) 197–212. doi:10.1016/j.matdes.2014.12.026.

[10] L. Susmel, D. Taylor, The Theory of Critical Distances to estimate the static strength of notched samples of Al6082 loaded in combined tension and torsion. Part II: Multiaxial static assessment, Engineering Fracture Mechanics 77 (3) (2010) 470–478. doi:10.1016/j.engfracmech.2009.10.004.

[11] L. Susmel, D. Taylor, The theory of critical distances to predict static strength of notched brittle components subjected to mixed-mode loading, Engineering Fracture Mechanics 75 (3-4) (2008) 534–550. doi:10.1016/j.engfracmech.2007.03.035.

[12] L. Susmel, D. Taylor, The Theory of Critical Distances as an alternative experimental strategy for the determination of KIc and ΔKth, Engineering Fracture Mechanics 77 (9) (2010) 1492–1501. doi:10.1016/j.engfracmech.2010.04.016.

[13] W. Li, L. Susmel, H. Askes, F. Liao, T. Zhou, Assessing the integrity of steel structural components with stress raisers using the Theory of Critical Distances, Engineering Failure Analysis 70 (2016) 73–89. doi:10.1016/j.engfailanal.2016.07.007.
[14] M. Peron, J. Torgersen, F. Berto, Rupture Predictions of Notched Ti-6Al-4V Using Local Approaches, Materials 11 (5) (2018) 663. doi:10.3390/ma11050663.
[15] A. Karolczuk, Non-local area approach to fatigue life evaluation under combined reversed bending and torsion, International Journal of Fatigue 30 (10-11) (2008) 1985–1996. doi:10.1016/j.ijfatigue.2008.01.007.
[16] L. Susmel, D. Taylor, The Modified Wöhler Curve Method applied along with the Theory of Critical Distances to estimate finite life of notched components subjected to complex multiaxial loading paths, Fatigue & Fracture of Engineering Materials & Structures 31 (12) (2008) 1047–1064. doi:10.1111/j.1460-2695.2008.01296.x.
[17] L. Susmel, The theory of critical distances: a review of its applications in fatigue, Engineering Fracture Mechanics 75 (7) (2008) 1706–1724. doi:10.1016/j.engfracmech.2006.12.004.
[18] L. Susmel, The Modified Wöhler Curve Method calibrated by using standard fatigue curves and applied in conjunction with the Theory of Critical Distances to estimate fatigue lifetime of aluminium weldments, International Journal of Fatigue 31 (1) (2009) 197–212. doi:10.1016/j.ijfatigue.2008.04.004.
[19] L. Susmel, D. Taylor, A critical distance/plane method to estimate finite life of notched components under variable amplitude uniaxial/multiaxial fatigue loading, International Journal of Fatigue 38 (2012) 7–24. doi:10.1016/j.ijfatigue.2011.11.015.
[20] B. Liu, X. Yan, An extension research on the theory of critical distances for multiaxial notchfatigue finite life prediction, International Journal of Fatigue 117 (2018) 217–229. doi:10.1016/j.ijfatigue.2018.08.017.
[21] M. Benedetti, C. Santus, Mean stress and plasticity effect prediction on notch fatigue and crack growth threshold, combining the theory of critical distances and multiaxial fatigue criteria, Fatigue & Fracture of Engineering Materials & Structures 42 (6) (2019) 1228–1246. doi:10.1111/ffe.12910.
[22] L. Bertini, C. Santus, Fretting fatigue tests on shrink-fit specimens and investigations into the strength enhancement induced by deep rolling, International Journal of Fatigue 81 (2015) 179–190. doi:10.1016/j.ijfatigue.2015.08.007.
[23] J. A. Araújo, F. C. Castro, S. Pommier, J. Bellecave, J. Meriaux, On the design and test of equivalent configurations for notch and fretting fatigue, Fatigue & Fracture of Engineering Materials & Structures 39 (10) (2016) 1241–1250. doi:10.1111/ffe.12435.
[24] C. T. Kouanga, J. D. Jones, I. Revill, A. Wormald, D. Nowell, R. S. Dwyer-Joyce, J. A. Araújo, L. Susmel, On the estimation of finite lifetime under fretting fatigue loading, International Journal of Fatigue 112 (2018) 138–152. doi:10.1016/j.ijfatigue.2018.03.013.
[25] C. Santus, Initial orientation of the fretting fatigue cracks in shrink-fit connection specimens, Frattura ed Integrità Strutturale 13 (2019) 442–450. doi:10.3221/IGF-ESIS.48.42.
[26] C. Santus, D. Taylor, M. Benedetti, Determination of the fatigue critical distance according to the Line and the Point Methods with rounded V-notched specimen, International Journal of Fatigue 106 (2018) 208–218. doi:10.1016/j.ijfatigue.2017.10.002.
[27] C. Santus, D. Taylor, M. Benedetti, Experimental determination and sensitivity analysis of the fatigue critical distance obtained with rounded V-notched specimens, International Journal of Fatigue 113 (2018) 113–125. doi:10.1016/j.ijfatigue.2018.03.037.
[28] M. Benedetti, C. Santus, Notch fatigue and crack growth resistance of Ti-6Al-4V ELI additively manufactured via selective laser melting: A critical distance approach to defect sensitivity, International Journal of Fatigue 121 (2019) 281–292. doi:10.1016/j.ijfatigue.2018.12.020.
[29] M. Benedetti, C. Santus, Statistical properties of threshold and notch derived estimations of the critical distance according to the line method of the theory of critical distances, International Journal of Fatigue 137 (2020) 105656. doi:10.1016/j.ijfatigue.2020.105656.
[30] P. Lazzarin, F. Berto, Control volumes and strain energy density under small and large scale yielding due to tension and torsion loading, Fatigue & Fracture of Engineering Materials & Structures 31 (1) (2008) 95–107. doi:10.1111/j.1460-2695.2007.01206.x.
[31] F. Berto, P. Lazzarin, J. R. Yates, Multiaxial fatigue of V-notched steel specimens: a non-conventional application of the local energy method, Fatigue & Fracture of Engineering Materials & Structures 34 (11) (2011) 921–943. doi:10.1111/j.1460-2695.2011.01585.x.
[32] M. R. Ayatollahi, F. Berto, A. Campagnolo, P. Gallo, K. Tang, Review of local strain energy density theory for the fracture assessment of V-notches under mixed mode loading, Engineering Solid Mechanics (2017) 113–132doi:10.5267/j.esm.2017.3.001.
[33] M. Benedetti, C. Santus, F. Berto, Inverse determination of the fatigue Strain Energy Density control radius for conventionally and additively manufactured rounded V-notches, International Journal of Fatigue 126 (2019) 306–318. doi:10.1016/j.ijfatigue.2019.04.040.
[34] F. Berto, A. Campagnolo, P. Lazzarin, Fatigue strength of severely notched specimens made of Ti-6Al-4V under multiaxial loading, Fatigue & Fracture of Engineering Materials & Structures 38 (5) (2015) 503–517. doi:10.1111/ffe.12272.
[35] F. Berto, A. Campagnolo, T. Welo, Local strain energy density to assess the multiaxial fatigue strength of titanium alloys, Frattura ed Integrità Strutturale 10 (2016) 69–79. doi:10.3221/IGF-ESIS.37.10.
[36] A. Carpinteri, F. Berto, A. Campagnolo, G. Fortese, C. Ronchei, D. Scorza, S. Vantadori, Fatigue assessment of notched specimens by means of a critical plane-based criterion and energy concepts, Theoretical and Applied Fracture Mechanics 84 (2016) 57–63. doi:10.1016/j.tafmec.2016.03.003.
[37] A. Campagnolo, G. Meneghetti, F. Berto, K. Tanaka, Crack initiation life in notched steel bars under torsional fatigue: Synthesis based on the averaged strain energy density approach, International Journal of Fatigue 100 (2017) 563–574. doi:10.1016/j.ijfatigue.2016.12.022.
[38] G. Meneghetti, A. Campagnolo, F. Berto, K. Tanaka, Notched Ti-6Al-4V titanium bars under multiaxial fatigue: Synthesis of crack initiation life based on the averaged strain energy density, Theoretical and Applied Fracture Mechanics 96 (2018) 509–533. doi:10.1016/j.tafmec.2018.06.010.
[39] C. Ronchei, A. Carpinteri, S. Vantadori, Energy Concepts and Critical Plane for Fatigue Assessment of Ti-6Al-4V Notched Specimens, Applied Sciences 9 (10) (2019) 2163. doi:10.3390/app9102163.
[40] R. O. Ritchie, Mechanisms of fatigue-crack propagation in ductile and brittle solids, International Journal of Fracture 100 (1) (1999) 55–83. doi:10.1023/A:1018655917051.

[41] C. Santus, D. Taylor, Physically short crack propagation in metals during high cycle fatigue, International Journal of Fatigue 31 (8-9) (2009) 1356–1365. doi:10.1016/j.ijfatigue.2009.03.002.
[42] J. C. J. Newman, Y. Yamada, Compression precracking methods to generate near-threshold fatigue-crack-growth-rate data, International Journal of Fatigue 32 (6) (2010) 879–885. doi:10.1016/j.ijfatigue.2009.02.030.
[43] H. C. Yu, K. Tanaka, Y. Akiniwa, ESTIMATION OF TORSIONAL FATIGUE STRENGTH OF MEDIUM CARBON STEEL BARS WITH a CIRCUMFERENTIAL CRACK BY THE CYCLIC RESISTANCE-CURVE METHOD, Fatigue & Fracture of Engineering Materials & Structures 21 (9) (1998) 1067–1076. doi:10.1046/j.1460-2695.1998.00105.x.
[44] Z. Hu, F. Berto, Y. Hong, L. Susmel, Comparison of TCD and SED methods in fatigue lifetime assessment, International Journal of Fatigue 123 (2019) 105–134. doi:10.1016/j.ijfatigue.2019.02.009.
[45] D. Liao, S.-P. Zhu, J. A. F. O. Correia, A. M. P. De Jesus, F. Berto, Recent advances on notch effects in metal fatigue: A review, Fatigue & Fracture of Engineering Materials & Structures 43 (4) (2020) 637–659. doi:10.1111/ffe.13195.
[46] L. Susmel, D. Taylor, A simplified approach to apply the theory of critical distances to notched components under torsional fatigue loading, International Journal of Fatigue 28 (4) (2006) 417–430. doi:10.1016/j.ijfatigue.2005.07.035.
[47] L. Susmel, D. Taylor, The Theory of Critical Distances to estimate finite lifetimeof notched components subjected to constant and variableamplitude torsional loading, Engineering Fracture Mechanics 98 (2103) 64–79. doi:10.1016/j.engfracmech.2012.12.007.
[48] R. O. Ritchie, F. A. McClintock, H. Nayeb-Hashemi, M. A. Ritter, Mode III Fatigue Crack Propagation in Low Alloy Steel, Metallurgical Transactions A 13 (1) (1982) 101–110. doi:10.1007/bf02642420.
[49] L. P. Pook, The Fatigue Crack Direction and Threshold Behavior of Mild Steel Under MixedMode I and III Loading, International Journal of Fatigue 7 (1) (1985) 21–30. doi:10.1016/0142-1123(85)90004-0.
[50] F. Berto, A. Campagnolo, Three-dimensional cracked discs under anti-plane loading and effects of the boundary conditions, International Journal of Structural Integrity 6 (4) (2015) 541–564. doi:10.1108/ijsi-02-2015-0007.
[51] L. P. Pook, A. Campagnolo, F. Berto, Coupled fracture modes of discs and plates under anti-plane loading and a disc under in-plane shear loading, Fatigue & Fracture of Engineering Materials & Structures 39 (8) (2016) 924–938. doi:10.1111/ffe.12389.
[52] F. Berto, Cracked components under anti-plane loading: recent outcomes and future developments, Frattura ed Integrità Strutturale 11 (2017) 475–483. doi:10.3221/IGF-ESIS.41.59.
[53] S.-P. Zhu, J.-C. He, D. Liao, Q. Wang, Y. Liu, The effect of notch size on critical distance and fatigue life predictions, Materials & Design 196 (2020) 109095. doi:10.1016/j.matdes.2020.109095.
[54] J.-C. He, S.-P. Zhu, D. Liao, X.-P. Niu, Probabilistic fatigue assessment of notched components under size effect using critical distance theory, Engineering Fracture Mechanics 235 (2020) 107150. doi:10.1016/j.engfracmech.2020.107150.
[55] M. Muniz-Calvente, A. M. P. de Jesus, J. A. F. O. Correia, A. Fernández-Canteli, A methodology for probabilistic prediction of fatigue crack initiation taking into account the scale effect, Engineering Fracture Mechanics 185 (2017) 101–113. doi:10.1016/j.engfracmech.2017.04.014.
[56] D. Liao, S.-P. Zhu, B. Keshtegar, G. Qian, Q. Wang, Probabilistic framework for fatigue life assessment of notched components under size effects, International Journal of Mechanical Sciences 181 (2020) 105685. doi:10.1016/j.ijmecsci.2020.105685.
[57] J.-C. He, S.-P. Zhu, D. Liao, X.-P. Niu, J.-W. Gao, H.-Z. Huang, Combined TCD and HSV approach for probabilistic assessment of notch fatigue considering size effect, Engineering Failure Analysis 120 (2021) 105093. doi:10.1016/j.engfailanal.2020.105093.
[58] M. Zappalorto, P. Lazzarin, J. R. Yates, Elastic stress distributions for hyperbolic and parabolic notches in round shafts under torsion and uniform antiplane shear loadings, International Journal of Solids and Structures 45 (18-19) (2008) 4879–4901. doi:10.1016/j.ijsolstr.2008.04.020.
[59] M. Benedetti, M. Dallago, C. Santus, Statistical significance of notch fatigue prognoses based on the strain-energy–density method: Application to conventionally and additively manufactured materials, Theoretical and Applied Fracture Mechanics 109 (2020) 102720. doi:10.1016/j.tafmec.2020.102720.
[60] E. Díaz-Francés, F. J. Rubio, On the existence of a normal approximation to the distribution of the ratio of two independent normal random variables, Statistical Papers 54 (2) (2012) 309–323. doi:10.1007/s00362-012-0429-2.